THE SEASONAL DYNAMICS OF EQUATORIAL SPREAD-F OVER

PUERTO MALDONADO – SOUTH AMERICA

By

ENOCH OUMA ASINO

A thesis submitted in partial fulfillment of the requirements for the degree of

Master of Science in Physics

SCHOOL OF BIOLOGICAL AND PHYSICALSCIENCES

MASENO UNIVERSITY

© 2015

ABSTRACT

Equatorial spread-F (ESF) phenomenon refers to intense post-sunset ionospheric irregularity that occurs around the geomagnetic equator due to perturbations in the ambient plasma. It has remained a very active area of ionospheric research for over eight decades now, owing to its adverse effects on trans-ionospheric radio signals. For many years, experiments have shown that spread-F can occur shortly after dusk and much later in the night, especially in the versatile equatorial ionosphere. Both pre-midnight and post-midnight ESF occurrences have been reported over the Indian and the South American sectors. Other studies have also endeavoured to explain the possible causes of these irregularities. However, not much work has been done to discover their persistence and seasonality over the equatorial region where their effect on radio signals is most severe. Globally, this situation has been aggravated by poorly distributed ionospheric measurements along the equatorial region. Therefore, using a recently installed ionospheric radio sounder, this study not only aims at establishing the seasonality and persistence patterns of both pre-MN and post-MN ESF, but also intends to characterize the diurnal and seasonal influence of the vertical $\mathbf{E} \times \mathbf{B}$ drift and electron density on ESF morphology over Puerto Maldonado (12.6°S, 69.2°W, dip lat. 0.1°N), an equatorial trough site that has in the past received very little attention. It further aims at revealing the unexplored effect of solar flux on ESF intensity. To achieve this, daily ionograms from the ionosonde have been analyzed on a 15 minute cadence, recording critical frequencies (foF2) and evaluating the vertical $\mathbf{E} \times \mathbf{B}$ drifts from virtual height (h'F2) measurements over the solar maximum period between December 2012 and November 2013. We further evaluated ESF percentage occurrence and measured the daily and monthly average spread ranges. The results revealed that the monthly occurrence trends were practically the same with both pre-midnight and post-midnight events having high occurrences of about 80-100% during summer months, and a minimum of about 25% during winter. This high summer prevalence is attributed to the effects of seasonal alignment of ITCZ with the magnetic field leading to the enhancement of gravity waves, thus increasing ESF occurrence. Pre-midnight ESF events lasted for ~4 hours longer in summer compared to post-midnight events which lasted 1-2 hours longer in winter and generally commenced earlier. Seasonal variations in strength of PRE drift and appearance of sporadic-E layer causes changes in meridional polarization and is thought to affect ESF occurrence duration. Summer and equinoctial months also recorded high foF2 and experienced high prevalence of ESF. Both daytime and the nighttime plasma drifts exhibited significant diurnal and seasonal dependence and portrayed a similar trend to that of the occurrence and development of ESF. The post-sunset PRE drift generally attained a threshold value of about 30m/s coinciding with the general start time of ESF when the daytime electric field orientation reverses with the shifting solar terminator. Solar flux indices showed a weak but significant direct correlation with ESF prevalence, but correlated inversely to the spread ranges a situation thought to be caused by the confinement of PRE drift peak and F-layer peak altitude to a narrow height range. The results of this study can be used to predict the ionosphere above Puerto Maldonado and further used to enhance the reliability of HF radio navigation and communication systems. These results will provide a guide to selecting the right frequency ranges to be used in trans-ionospheric communication.

CHAPTER ONE

INTRODUCTION

1.1 Photo-ionization and Recombination in the Ionosphere

Above the stratosphere, beyond an altitude of ~50 km, the atmosphere comprises of a high density of free electrons and free ions existing in a quasi-neutral background commonly referred to as the ionosphere (Rees, 1989). These free electrons and ions are products of an energetic photo-ionization by ultraviolet (UV) rays and X-rays emitted by the Sun, during which neutral atoms absorb photon energy, E given in the form:

$$E = h\frac{c}{\lambda} \quad\text{...} 1$$

where h is the Plank's constant, c the velocity of light, and λ the wavelength of the incident solar radiation. The equation gives the ionization energy E of a radiation of wavelength λ. This energy causes the neutral atoms in the ionosphere to be stripped of electrons giving rise to free ion-electron pairs in a process known as photo-ionization. To elaborate this process, Figure 1 shows a simplified scheme of photo-ionization by Zolesi and Cander (2014) demonstrating how electrons are dislodged from their neutral atoms by the energy of UV rays from the Sun, producing ions and free electrons in the process.

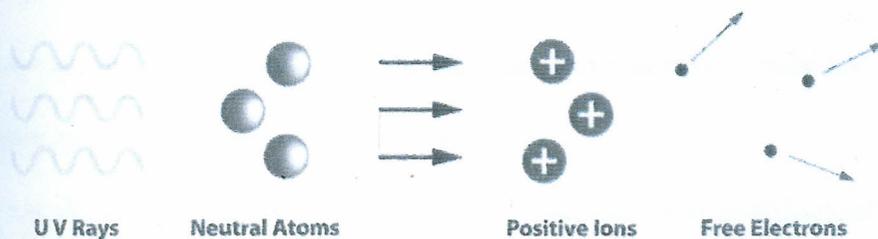UV Rays   Neutral Atoms   Positive Ions   Free Electrons

Figure 1: A simplified scheme of photo-ionization showing how UV rays knock off electrons from neutral atoms in the ionosphere.

The amount of energy required for the ionization varies with different components of the atmosphere. Other than photo-ionization of mono-atomic species, dissociative ionization also occurs in the ionosphere when various molecular species like oxygen and nitrogen undergo photo-ionization (Rees, 1989). This process, depending upon the constituent of the ionosphere, requires different amount of energy as is tabulated in Table 1. The table shows that the photo-ionization energy, expressed in electron-volt (eV) or simply in terms of the wavelength λ given in nanometers (nm) or Angstrom ($\text{Å} = 10^{-10}$ m), is not only dependent on the chemical component of the ionosphere but also on the wavelength of incident solar radiation. It is therefore predominantly a daytime phenomenon.

Table 1: Variation of ionization/dissociation energies and radiation wavelengths with different chemical species in the ionosphere

Species	Ionization		Dissociation	
	V_p (eV)	λ (Å)	V_p (eV)	λ (Å)
N_2	15.58	796	9.76	1270
O_2	12.08	1026	5.12	2422
O	13.61	911		
N	14.54	853		
NO	9.25	1340	6.51	1905
H	13.59	912		
He	24.58	504		

Besides, the production of ion-electron pairs further depends upon the probability of collision or interaction between radiation photons and neutral atoms (Zolesi & Cander, 2014). This implies that ionization is not only proportional to the abundance of a given chemical component, but also to the intensity and wavelength of solar radiation.

During the night, recombination dominates other chemical processes of the ionosphere. This refers to the reverse phenomenon of photo-ionization, when the once free electrons and the

positive ions recombine again to produce neutral atoms (Buchert, 2007). Recombination can either be radiative or dissociative.

In radiative recombination, electrons undergo a direct interaction with the positive ion to produce a neutral atom or molecule dissipating excess energy in the process while in dissociative recombination, positive ions produced during photo-ionization first interact with neutral diatomic molecules and then attach to the free electrons to produce two neutral atoms (Rees, 1989). Recombination occurrence probability is not only dependent upon the ionospheric density of the chemical element and on the electron affinity of the element, but also on the electron density of the ionosphere (Zolesi & Cander, 2014). Recombination is thus dependent on ionospheric electron density which is majorly controlled by the solar radiation energy.

Consequently, solar flux measurement is found to be highly correlated with many ionospheric parameters because it is associated to solar X-ray and ultraviolet fluxes (Buchert, 2007). Qualitative study of the ionosphere therefore demands a detailed knowledge of the characteristics and behaviour of this critically significant wavelength region of the solar flux. The daily full-disk solar flux on a wavelength of 10.7 cm (2800MHz), measured with a reflector of 1.8m diameter near Ottawa, Canada at about 1700 UT, is one of the most commonly used and the most available indicators of the general level of solar activity (Davies, 1989). These measurements are obtained using the EUVAC Solar Flux Model which applies 37 wavelength intervals over a range of between 5 to 105 nm to provide an estimate for the un-attenuated solar flux (F10.7) variation for any given period. F10.7 is the 10.7 cm solar radiation flux given in solar flux units, (SFU) which is equivalent to $10^{-22} Wm^{-2}Hz^{-1}$ obtained when radiation frequency is at 2800MHz (Schunk & Nagy, 2009). Solar flux varies from a minimum of about 65 SFU at

1.2 Radio Reflection

The vertical structure of the ionosphere comprises of four regions according to ion constituent and associated chemistry (Davis, 1989). These are the D (60 − 90 km), E (90 − 140 km), F1 (140 − 210 km) and F2 (above 210 km) regions. The lower regions of the ionosphere lie in a comparatively denser atmosphere than the upper F1 and F2 layers. The ionosphere, to a minor extent, further stretches over high altitudes courtesy of corpuscular ionization to encompass upper atmospheric regions such as the mesosphere, thermosphere, and exosphere (Zolesi & Cander, 2014).

For this reason, a high or relevant density of free electrons and free ions per se does not provide clear-cut defining characteristic of the ionosphere since electrons and ions are present at every altitude in both lower and upper atmospheres. Therefore, according to Zolesi and Cander (2014), a more practical definition of the ionosphere, originating from the first application of long distance radio communications, is that region of the atmosphere in which the density of ionization is adequate to deflect radio waves in the 2–30 MHz range. Equation 2 is a simplified Appleton-Hartree equation that gives the general value of the refractive index μ in collisionless plasma assuming a zero magnetic field as:

$$\mu^2 = 1 - \frac{\omega_p^2}{\omega^2} \quad \dots\dots\dots\dots\dots\dots\dots\dots\dots\dots\dots\dots\dots\dots\dots\dots\dots\dots\dots\dots\dots\dots\dots\dots\dots 2$$

where ω_p is the plasma frequency while ω is the frequency of the propagating radio wave (Schunk& Nagy, 2009). This equation implies that increase in electron density leads to a higher frequency of radio waves deflected by the ionosphere if analyzed in view of the fact that electron plasma frequency is a factor of plasma density (Buchert, 2007).

1.3 Ionospheric Dynamics

The variability of the electron density in the ionosphere exudes both diurnal, seasonal, and latitudinal dependence with geomagnetic activities, neutral winds, and solar cycle also playing a major role in determining the electron concentration of the ionosphere (Zolesi & Cander, 2014).
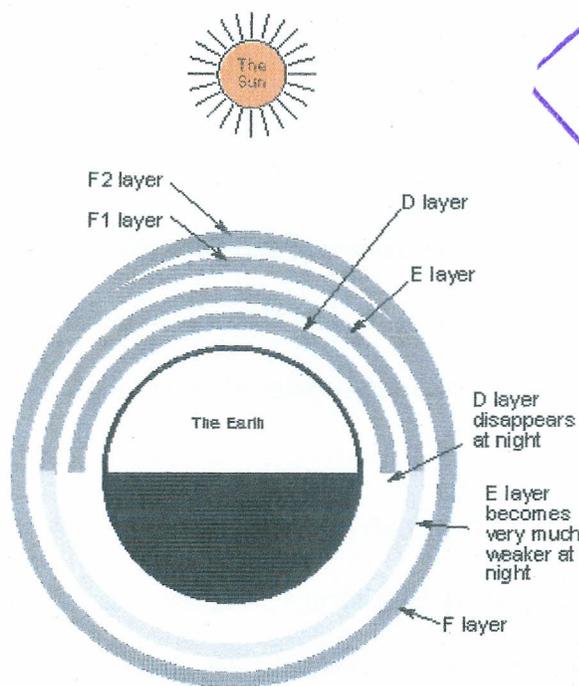
Figure 2: A simplified view of the regions in the ionosphere showing their variations during both day and night

Figure 2 shows an exemplification by (Poole, n.d.) of the diurnal and nocturnal structure of the ionosphere. During the day, the ionosphere separates into its constituent regions depending on the local time as indicated in the figure. D region vanishes while E weakens significantly due to rapid recombination during post sunset hours. However, F1 region becomes much weaker and eventually merges with F2 during the night as shown in Figure 2. In fact, the average lifespan of an electron in D is essentially quite unstable and not yet determined while in E, F1 and F2

regions it lasts 1 second, 1 minute, and 20 minutes respectively (Bhattacharya & Pandit, 2014). Wyman, (2009) asserted that the E region and the F1 region undergo relatively greater variations in electron density between daytime and nighttime than does the upper F2 region. It is therefore the principle reflecting region for high frequency (HF) radio communications and is responsible for most sky wave propagation of radio waves largely due to its 24 hour presence. It is however the most variables of all the regions and the most difficult to predict.

Diurnally, the daytime ionospheric electron densities are greater than those of the nighttime and also larger during the solar maximum than at solar minimum due to increased ionization among other influencing factors. According to Wyman (2009), ionospheric electron densities are greater by a factor of two to four at solar maximum than at solar minimum. There is only one maximum and one minimum in the 11 year solar cycle. These electron density variations are further controlled by the changes in solar declination which varies annually from $23.45^{o}S$ to $23.45^{o}N$.

The rising of the Sun causes a west-east (zonal) electric field **E** with an increase in ionization in the east. On the other hand, the geomagnetic field **B** runs horizontally, basically with a northward orientation at the low latitudes compared to middle and high latitudes. This results in a vertical electromagnetic plasma drift commonly known as **E** x **B** drift or electric field drift which is strongest at the equatorial regions where the **B** and **E** fields are essentially perpendicular (Rishbeth, 2000). This force results in the lifting of the F region by a velocity V known by the familiar form shown in Equation 3:

$$V = \frac{E \times B}{B^2} \quad \dots\dots\dots\dots\dots\dots\dots\dots\dots\dots\dots\dots\dots\dots\dots\dots\dots\dots\dots\dots\dots\dots\dots\dots\dots\dots\dots\dots 3$$

where B^2 is the square-modulus of the geomagnetic field flux **B**. Plasma is thus driven to high altitudes during the day then diffuses downwards and outwards along the geomagnetic field

6

lines towards north and south causing a meridial electric field and depleting the equatorial plasma in a phenomenon known as the equatorial fountain effect. This leads to the stockpiling of plasma or formation of equatorial crests at about 20° north and south of the magnetic equator leading to the Appleton Anomaly or Equatorial Ionization Anomaly (EIA) with the equatorial trough at its centre (Liu & Wan, 2001). The nighttime electron densities reach a minimum at around 60° latitude north and south of the geomagnetic equator, which is called the mid-latitude trough (Wyman, 2009). Radio communicators near the equator during the day and around 60° latitude at night should be wary of these phenomena.

At sunset, the electric field orientation reverses with the shifting solar terminator (the day-night boundary) and rising of the F region is thus anticipated. However, it has been observed that it rapidly rises momentarily in what is commonly referred to as the pre-reversal enhancement (PRE) before commencing a gradual descent (Rishbeth, 2000). This drift leads to an upward polarization of charges creating a vertical electric field which introduces an east-west plasma drift that further complicates the ionospheric dynamics.

In general, drift dynamics, diurnal and seasonal solar flux variations coupled with neutral wind activities are some key drivers which constantly modify the F region plasma density resulting in irregularities with wide ranges of magnitude and amplitude at almost all altitudes (Liu & Wan, 2001). However, the low-latitude regions experience the most severe electron density fluctuations and as such exhibits very intense irregularities.

1.4 Equatorial F-Region Irregularities

Plasma irregularities and inhomogeneities are predominantly a post-sunset phenomenon in the equatorial F-region ionosphere which poses greatest nightmare to radio communication and navigation systems due to the complex and dynamical nature of the instabilities (Zolesi &

7

Cander, 2014). The horizontal geomagnetic field lines which are perpendicular to gravity at the magnetic equator interplay with both the prevailing natural wind and the background electric field, to produce plasma irregularities which develop a unique equatorial phenomenon. This phenomenon is referred to by the generic name equatorial spread F (ESF) owing to the first recorded spread they caused on ionograms at Huancayo, Peru (Pezzopane, et al., 2013). ESF irregularities are associated with significant depletion in the background electron density and are magnetic field aligned with characteristic sizes from a few tens of centimeters to several kilometers.

Along the magnetic equator, the post-sunset F-region rapidly ascends to higher altitudes. This coupled with the effect of increased rate of recombination of the lower layers of the ionosphere leads to a highly depleted bottomside with respect to the topside causing a steep plasma density gradient. Figure 3 is a two dimensional simulation of ESF formation by Joyce and Krall, (2012) showing regions of different electron densities and how the lower less denser regions rise above the heavier layers causing depletions in the F-region structure.
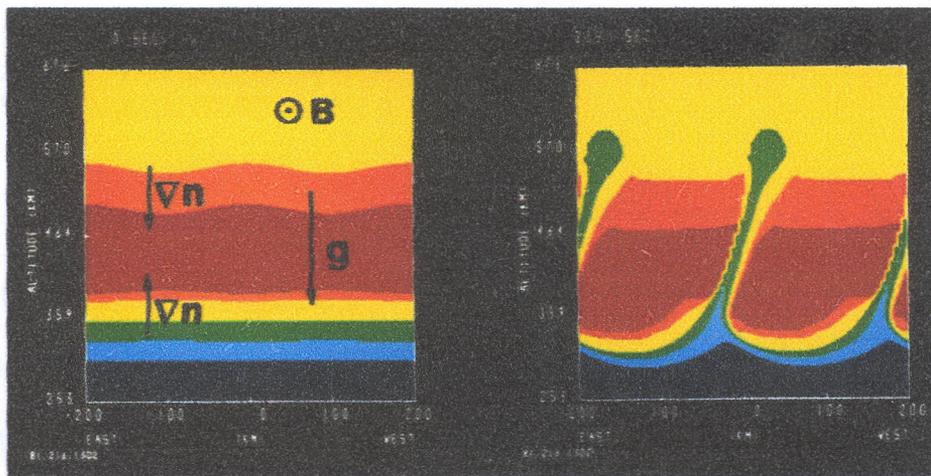

Figure 3: A two dimensional simulation of ESF formation showing the interplay between the geomagnetic fields, gravity waves and density variations where n is plasma density and g is gravity.

These conditions result in the formation of ESF which is thought to be further shaped and developed by the Rayleigh–Taylor (RT) instability mechanisms (Rao, Ram, Niranjan, & Prasad, 2006). Other authors (e.g. Ram, et al., 2006) have also asserted that a combination of post-sunset **E** x **B** drift and RT instability constitute the basic mechanism for ESF initiation. In fact, sudden decay in ionospheric electron density, the reversal of zonal electric field orientation at sunset, the orthogonal coupling of the **E**-field and **B**-field at the magnetic equator, together with the effects of neutral wind circulation leads to intense pre-reversal enhancement (PRE) resulting in a significant increase in vertical **E** x **B** drift and the initiation of ESF (Rishbeth, 2000; Pezzopane, et al., 2013).

The ESF instability growth is driven by the RT process through the collisional interchange instability with the characteristic growth rate which reflects the combined actions of gravity, plasma drift, neutral wind and electric field. Equation 4 is a convenient expression for the growth rate γ_g as was derived by Zalesak and Ossakov (1982) and further adapted by Sultan (1996):

$$\gamma_g = \frac{\Sigma_P^F}{\Sigma_P^F + \Sigma_P^E}\left(V_P - U_n^P - \frac{g_L}{v_{in}^{eff}}\right)\frac{1}{L_n} - R_T \quad \dots\dots\dots\dots\dots\dots\dots\dots\dots\dots\dots\dots\dots\dots\dots\dots\dots\dots \quad 4$$

where g_L represents the downward acceleration due to gravity, V_P is the vertical component of plasma drift due to the zonal component of the electric field **E** at the magnetic equator, U_n^P is the vertical component of neutral wind velocity perpendicular to **B**, and v_{in}^{eff} is the effective, flux-tube integrated, F-region, ion-neutral collision frequency weighted by number density in the flux tube. L_n is the scale length of the vertical gradient of the flux-tube integrated plasma density measured at the equator. R_T is the flux-tube integrated recombination rate (Basu,

1997). Σ_P^F and Σ_P^E are the contributions to Pedersen conductivity from the E and F regions, respectively. In the bottomside of the F-layer in the post-sunset ionosphere the L_n is positive and eastward components of $\mathbf{E}$ and downward components of U_n^P contribute to a positive growth rate γ_g. Growth periods, $1/\gamma_g$ are generally about 10 min, and large-amplitude irregularities develop over several growth periods. Since g_L and $\mathbf{B}$ are constants at a given location, the RT growth rates are controlled by the daily and seasonal variability of $\mathbf{E}$, U_n^P, Σ_P^F, Σ_P^E, v_{in}^{eff} R_T, and by the height of the F-layer which affects the flux-tube integrated quantities (Gentile et al., 2006). All these parameters are directly affected by the solar flux and ambient electron density.

Theoretically, there is a relatively short time window when the instability can grow according to the above formula. Shortly after the sunset, when the electric field strengthens, the ionosphere rises up and instabilities form. As the vertical plasma drift subsides and later reverses, the formation of RT instabilities then stops. However, experimentally, the ESF have been observed both shortly after dusk and much later in the night (e.g. Dabas, et al., 2007).

Both pre-midnight (pre-MN) and post-midnight (post-MN) occurrences of ESF have been reported in certain low-latitude regions (Yizengaw, Moldwin, Sahai, & de Jesus, 2009), but not much work has been done to discover their seasonality and persistence. Dabas et al., (2007) calculated the pre- and post-midnight ESF prevalence over Trivandrum, India at 91.7% and 8.3% respectively. Longitudinal variations, as well as equinoctial and hemispherical asymmetry in ESF occurrence have been reported by Pezzopane et al., (2013) and other references therein confirming the complexity of the dynamics and processes that lead to the initiation and development of ESF over different equatorial sites.

Many studies (e.g. Rishbeth, 2000; Liu & Wan, 2001) have also reported the various effects of longitudinal, latitudinal, temporal, seasonal, solar and geomagnetic activity variation

10

on ESF occurrence and showed that regional characterization of ESF is an important key to unlocking its global behaviour. Dabas et al., (2007) while studying the seasonal behaviour of pre-MN and post-MN ESF over the Indian equatorial sector only considered drift dependence while Chapagain et al., (2009) considered onset heights, solar flux, drifts influence on ESF prevalence over Jicamarca, Peru. Very little has however been done to show the effect of solar flux on ESF intensity.

Therefore, studies of occurrence and evolution of ESF above a specific region require a detailed characterization of the major drivers. An analysis on the variability of drivers provides an opportunity for identification of the precursor signatures which is key to the predictability of ESF. Such studies should be done with respect to local-time variability which has revealed the peculiar occurrence of both pre- and post-MN ESF over the equatorial region (Dabas, et al., 2007; Yizengaw, et al., 2009). It is only after this that the seasonality and climatology of ESF can be obtained and its predictability achieved. However, none of these studies have endeavoured to establish the ESF dynamics by the pre-MN and post-MN occurrence approach. The effects and influences of major ESF drivers on the duration of spread occurrence (persistence) and on the intensity of spread (spread range) has not been examined to provide a proper understanding of the evolution of ESF over the low-latitude regions. Worsened by the rather scarce coverage of the equatorial regions with routine ionospheric monitoring, the ESF observations have been performed only at selected locations, among which, Jicamarca for example, has seen a lot of studies, while other regions nearby have been largely devoid of the ionospheric measurements. There have been reports (e.g. Pezzopane, et al., 2013; Dabas, et al., 2007), however, that ESF statistics can differ significantly even within the same geographical region.

11

1.5 Problem Statement

For many years, experiments have shown that spread-F can occur shortly after dusk and much later in the night, especially in the versatile equatorial ionosphere. Both pre-MN and post-MN occurrences have been reported over the Indian and the South American sectors. However, not much work has been done to discover their persistence and seasonality over the equatorial region where their effect is most intense. Globally, this situation has been aggravated by poorly distributed ionospheric measurements along the equatorial region.

Therefore, using an ionospheric radio sounder, the current study not only aims at unearthing the seasonality and persistence patterns of both pre-MN and post-MN ESF, but also intends to characterize and establish the diurnal/seasonal influence of the vertical $E \times B$ drift and electron density (inferred from foF2 measurements) on ESF morphology over Puerto Maldonado ($12.6^{o}S$, $69.2^{o}W$, dip lat. $0.1^{o}N$), an equatorial trough site that has largely been ignored by researchers. It will further reveal the unexplored effect of solar flux on pre- and post-MN ESF intensity (spread range) and occurrence.

1.6 Objectives of the Research

This study generally aims at outlining the annual variability of ESF over Puerto Maldonado and establishing possible influences of its major drivers with an intention of improving on its predictability.

Its specific objectives include;

1. To establish the seasonal occurrence and persistence patterns of pre-MN and post-MN equatorial spread-F over Puerto Maldonado.

2. To characterize and identify the influence of vertical $E \times B$ drift velocity and foF2 on ESF variability.

12

3. To establish the correlation between solar flux and ESF intensity over Puerto Maldonado.

1.7 Hypothesis

This study scientifically attempts to provide proof to the belief that;

1. There is no well-pronounced seasonal variability of the equatorial spread-F over the Puerto Maldonado.

2. Spread-F occurrence over Puerto Maldonado has no distinct difference from those over other equatorial regions.

3. There is no direct influence of solar flux on the ESF spread intensity.

1.8 Justification of the Study

Today, with increase in global interaction, radio communication with satellites (HF radios), positioning/navigation (GPS L-band) applications, and spacecraft control have become so vulnerable to ionospheric variations. These variations could potentially affect or disrupt the system performance due to the effects of ionosphere on radio signals (Carrano & Groves, 2010; Shi, et al., 2011). Therefore, research on characteristics and variations of spread F has an important significance for science and for GNSS applications especially in aviation industries, where accuracy and reliability is often a vital issue. The findings of this study are important in advising telecommunication, aviation and navigation industries on the optimal frequencies to use during different seasons and in various local times.

The driver dynamics and precursor signatures are also key components in forecasting the behaviour and changes in the ionosphere. This helps in either flagging the use of certain frequencies or sending warnings under fluctuating ionospheric conditions. This will help save lives and property hence reducing risks in HF radio, navigation and GNSS related applications. However, at present we are limited by the data availability from any equatorial VIPIR station.

13

Puerto Maldnonado sounder in fact had the most regular observations starting from October 2010, other sounders from LISN network operated for shorter periods of time.

1.9 Limitations of the Research and Possible Remedies

Although a seasonal study is useful in revealing the annual ESF occurrence trend hence enabling its predictability, such studies may still be inadequate with reference to the eleven year solar cycle and its distinctive features for both solar maxima and minima. Therefore, ESF occurrence and seasonality study done over a duration of eleven years might reveal much more information with regard to the climatological effects of solar cycle on the dynamics of this equatorial irregularity.

CHAPTER TWO

LITRATURE REVIEW

2.1 Review of ESF and its Drivers

A review by Rishbeth, (2000) asserted that within a few degrees of the geomagnetic equator, the ionosphere has peculiar features that cannot be found elsewhere. Since its discovery in the 1930s, spread-F has been central to ionospheric research for about eight decades after a mysterious spread in ionogram traces was first observed over an equatorial site in Huancayo, Peru (Pezzopane, et al., 2013). With the current advancements in technology, spread-F poses potentially adverse economic threat to critical systems such as navigation, communication, electrical power distribution grids, among others (Carrano & Groves, 2010; McDaniel, 2009). A consorted campaign has thus been laid out both by experimental and theoretical scientists to unravel the physical mechanisms responsible for the ESF phenomenon as an attempt to improve its predictability and thus reduce the extent of possible risks. This has in the recent times led to a dramatic increase in the understanding of diurnal, seasonal, and climatological behaviour of ESF since its discovery. Endeavours have also been made (e.g. Rao, et al., 2006) to establish the ESF precursor signatures in a bid to improve its predictability. However, this effort has often been complicated by the dynamic nature of these irregularities and by the combined effects of their drivers (solar flux, $E \times B$ drift, geomagnetic conditions, and plasma density variations) and spatial-temporal differences (latitudinal, longitudinal, local time, and seasonal) as reported by Rishbeth, (2000) and Liu and Wan, (2001).

On geomagnetic field and solar activity influence, Rabiu, Mamukuyomi, and Joshua (2007) theoretically studied the variability of equatorial ionosphere and found out that for both low and high solar activity periods, the ionospheric dynamics can be uniquely inferred from

15

geomagnetic field measurements. Elsewhere, Engavale, Jeeva, Nair, and Bhattacharyya, (2005) investigated the solar flux (F10.7) dependence on scintillation patterns produced by equatorial spread-F and revealed that during the initiation phase of ESF development, the irregularity lacks much variability while further development or evolution depends upon other factors but not on solar flux. This called for an in-depth study on the initiation and development of ESF to reveal factors that may be responsible for the evolution or inhibition of ESF.

Therefore, Oyekola and Oluwafemi, (2009) studied the parameters influencing the evolution and inhibition of post-sunset plasma instability over Ouagadougou (dip lat. 3°N) and found out that the peak F-layer height and vertical plasma drift velocity decreased appreciably with increase in solar flux during low solar activity periods while there was no significant relationship during high solar activity (F10.7 > 200SFU). However, the effect of solar flux on intensity of the irregularity was not shown. Nevertheless, they further pointed out that the vertical $E \times B$ drift and the nighttime peak F-layer during high solar activity periods was affected by the meridional neutral wind, while the inhibition of irregularity development during high solar flux was due to the confinement of PRE drift peak and the F-layer peak altitude to a narrow range, but failed to show the seasonal variability and persistence on these irregularities. Another study by Yizengaw, et al., (2009) while acknowledging PRE as one of the prime triggering agents of post-sunset ESF and that sudden change in electric field direction from westwards to eastwards is the cause of post-midnight irregularities during active solar conditions, pointed at the need for research on the post-MN irregularities that occur during quite solar conditions.

Latitudinal, longitudinal, and seasonal variations in ESF have also been studied by Pezzopane, et al., (2013) by comparing ESF occurrences over five equatorial stations on different equinoctial seasons and separated in longitudes and latitudes. Their results showed major

16

seasonal, latitudinal and longitudinal variations in ESF occurrence with the stations showing varied ESF occurrence patterns pointing to the need for characterization of ESF over individual regions. Further seasonal and longitudinal variability of post-MN ESF with peak in June solstice have also been reported by Yizengaw, et al., (2013) who concluded that both post-MN and pre-MN ESF are initiated by similar mechanisms and that the frequent appearance of sporadic E during June solstice causes eastward polarization in electric field resulting in quite time post-MN ESF. Elsewhere, after considering normalized changes in foF2 and total electron content (TEC) values, Xenos, (2002) also noted that the two quantities have a relational coefficient which is controlled by these seasonal variations. Therefore, seasonal, longitudinal, latitudinal, and diurnal variations not only affect vertical drift and foF2, but also the occurrence and evolution/development of ESF. Researchers (e.g. Rao, et al., 2006; Dabas, et al., 2007; Chapagain, et al., 2009) have for this reason embarked on regional studies of seasonality and climatology of ESF by creating an understanding of the precursor signatures emanating from the drivers.

For instance, a systematic study by Rao, et al., (2006) aimed at quantitatively identifying the precursors for VHF scintillation and ESF irregularities over an Indian equatorial crest station (Waltair, dip lat. 20°N) during high and low solar sunspot years revealed that the percentage occurrence of these irregularities had a good correlation with the monthly mean vertical drift velocities both in solar maximum and solar minimum. A further comparison with results from other nearby equatorial station revealed unexplained differences in seasonal variation of irregularities. They also noted that the threshold **E** x **B** drift velocity that triggers the onset of ionospheric irregularities over Waltair is 30m/s during high solar activity periods while it drops to 20m/s during the low solar activity periods. They further noted that the threshold PRE drifts

17

were well defined in equinoctial months, less in winter and least in summer solstices. However, having shown the variations in prevalence, not much was done to show the seasonal variations in persistence and intensity of the irregularities.

Elsewhere, from a study on the climatology of post-sunset ESF over Jicamarca (dip lat. $0.5^{\circ}N$), using an eleven-year dataset from coherent and incoherent scatter radar, Chapagain, et al., (2009) observed that ESF onset heights had a strong correlation to the evening velocity vortex and depended on the solar cycle while the ESF onset times largely remained unvaried. According to their results, equinoctial ESF onset occurs close to drift reversal times when the F-layer has attained its peak height. Chapagain et al., (2009) reported the maximum ESF occurrence at Jicamarca during the December solstice of 88% as opposed to the June solstice minimum of 32%. However, other than analyzing the onset times of these irregularities, their persistence was not considered, and like Oyekola and Oluwafemi, (2009), they did not show the seasonal variability of post-MN irregularity occurrence even after acknowledging their occurrence.

Finally, Dabas, et al., (2007) used digisonde data collected for a period of one year over the Indian low-latitude sector to study the occurrence seasonality and predictability of ESF. They grouped the twelve months into winter (May, Jun, Jul, & Aug), summer (Jan, Feb, Nov, & Dec) and the equinoctial months (Mar, Apr, Sep, & Oct) and discovered that at the equatorial station (Trivandrum, dip lat. $8.2^{\circ}N$), both pre-MN and post-MN ESF occurrence had large seasonal variations. Their study showed that maximum ESF prevalences for summer and winter were about 83% and 30% respectively with equinoctial symmetry and solsticial asymmetry in occurrence. On latitudinal variation, they concluded that except in the winter months, the spread F at Trivandrum (dip lat $8.2^{\circ}N$), Waltair (dip lat $17.7^{\circ}N$), and Delhi (dip lat $28.6^{\circ}N$) are observed

18

only when equatorial $E \times B$ drift is more than about 15 m/s (325 km), 20 m/s (350 km) and 25 m/s (375 km), respectively. The physical mechanism for this difference is not yet understood. Furthermore, other than the latitudinal variations, not much was stated about the differences in ESF occurrence percentages and durations of occurrence.

This study therefore aims at using a Vertical Incidence Pulse Ionospheric Radar (VIPIR) ionosonde to reveal and explain the seasonality in occurrence and persistence of both pre- and post-MN ESF over the equatorial trough, a region with the greatest ESF variability. Puerto Maldonado (dip lat. 0.1°N) offers a good site for this study due to its close proximity to the geomagnetic equator. Even though studies (e.g. Oyekola, & Olowafemi, 2009; Yizengaw, et al., 2009; Pezzopane, et al., 2013) have endeavoured to show the effects of major drivers on ESF percentage occurrence over certain regions, the effect of solar flux on intensity (spread range) of ESF remains largely unexplored in this region. Therefore, we have not only focused on the diurnal and seasonal behaviour of vertical $E \times B$ drift and foF2 over Puerto Maldonado, but also on establishing the effects of F10.7 variability on occurrence and intensity of ESF. We have then proceeded to carry out a comparative analysis between our observation and published reports from two other equatorial trough stations. These are Jicamarca (dip lat. 0.5°N and close to Puerto Maldonado) and Trivandrum (dip lat. 8.2°N and far from Puerto Maldonado) which are respectively found in the Peruvian sector and the Indian sector.

2.2 VIPIR Ionosonde Review

The original NOAA HF Radar developed the 1970's and later known as the Dynasonde was designed to be a flexible general purpose tool for taking ionospheric research measurements (Grubb, Livingston, & Bullet, 2008). This radar evolved from the previous gigantic and expensive pulse-based ionosondes which were developed during the world wars and embodied

the capabilities of Dynasonde and Kinesonde phase coherent systems which were earlier developed in Boulder Laboratories (Bibl, 1998). However, with the later emergence of digital and analogue technology, the entire complex return-signal synthesis had to be digitized using by multiple parallel receiver channels to enable simultenous measurement of signals from an array of spaced receiving antennas (Bibl, 1998; Grubb, 2008). New measurement techniques were adopted and standards for improved electromagnetic compatibility with other HF and MF spectrum services were set by the introduction of matched transmitter and receiver signal shaping (Grubb, 2008). So even though these modified systems are still in use today, their general architecture is largely old and out of touch with the fast-changing present-day technology. This culminated into the birth of VIPIR ionosonde.

The VIPIR ionosonde is the latest design of ionospheric HF radar built with modern digital electronics and developed by Scion Associates (Bullet, Malagnini, Pezzopane & Scotto, 2010). This instrument operates in the medium frequency (MF) and high frequency (HF) bands of between 0.5MHz to 30MHz and has the enormous potential of scanning the ionosphere in different modes including high temporal, fast sweep, and special resolution modes to view the E and F regions (Krishna, Valladares, Doherty, Bullet, & Livingston, 2011). It readily relates the local ionospheric electron density n_e at the point of incidence to the local plasma frequency (Bullet, 2013), which is equivalent to the sounding frequency, according to Equation 5:

$$n_e = \frac{\varepsilon_0 m}{e^2}(2\pi f_p)^2 \approx 1.24 \times 10^{-2} f_p^2 \dots\dots\dots\dots\dots\dots\dots\dots\dots\dots\dots\dots\dots 5$$

where f_p is the plasma frequency in Hertz, and n_e is electron density in m^{-3}. This instrument is thus capable, not only of determining the reflection heights of various signal frequencies, but also actualizes the possibility of reconstructing the altitude profile of the bottomside ionosphere. It is through this reconstruction that the ionograms are obtained in terms

of plot showing electron density on a grid of virtual height of the ionosphere in kilometers against frequency in Megahertz.

Compared to other ionospheric sounders that ever existed before it, this radar provides a high resolution and thus a clear distinction between the ordinary and the extra-ordinary polarization traces in ionograms (Grubb, et al., 2008). Ionograms are then analyzed in temporal sequence to reveal most ionospheric parameters. For this reason VIPIR is designed to meet high performance and flexibility needs with the ability to record ionograms every 6 seconds (Krisma, et al., 2011). By transmitting eight frequencies with 128 repeats, this sounder is able to observe each frequency over 0.064 seconds sampling interval (Bullet, et al., 2010).

Therefore, bearing in mind that the lifetime of an electron in this region is only about 20 minutes (Bhattacharya & Pandit, 2014), the fast-sweep capability and the agility of this sounder makes it effective and reliable for carrying out F-region observations. Secondly, the ability of this instrument to operate in the MF and HF bands of between 0.5MHz to 25MHz (Krishma, et al., 2011) makes it appropriate for use in bottomside ionospheric research owing to the fact that the ionospheric density of ionization is only adequate to deflect radio waves in the 2–30 MHz range (Zolesi & Cander, 2014).

The VIPIR ionosonde therefore suits our study owing to its state-of-the-art technology, flexibility and reliability, and its technological adaptability to execute multiple simultaneous experiments, thus enabling pulse-to-pulse routine measurements with dedicated special operational modes (Valladares & Doherty, 2011). The first VIPIR ionosonde in South America was temporarily installed in Jicamarca (dip lat. 0.5°N) and was later relocated to Puerto Maldonado (dip lat. 0.1°N) in 2010, where a world-class log-periodic transmitting antenna was then erected (Valladares & Doherty, 2011). This was done under the umbrella of Low-latitude

21

Ionospheric Sensor Network (LISN) with one of its major objectives being the provision of necessary tools for studying ionospheric disposition and the seeding conditions for the initiation of ESF (Valladares & Chau, 2012).

CHAPTER THREE

METHODOLOGY

3.1 Installation and Operation of VIPIR Ionosonde

Historically, ionosondes have been the first instruments to study the ionosphere, some of which began routine observations in from 1930s (Bible, 1998). The ionospheric radar in Puerto Maldonado (12.6°S, 69.2°W, dip lat. 0.1°N) is a ground-based world-class sounder that sits on an area of about 10 acres of land. It has the ability to measure the ionospheric virtual heights and plasma density profiles among other uses (Bullet, 2011). Figure 4 shows the architectural plan by Bullet, (2013) used in the installation of this VIPIR station and the receiver-transmitter arrays designed to achieve optimum operation at equatorial sites.
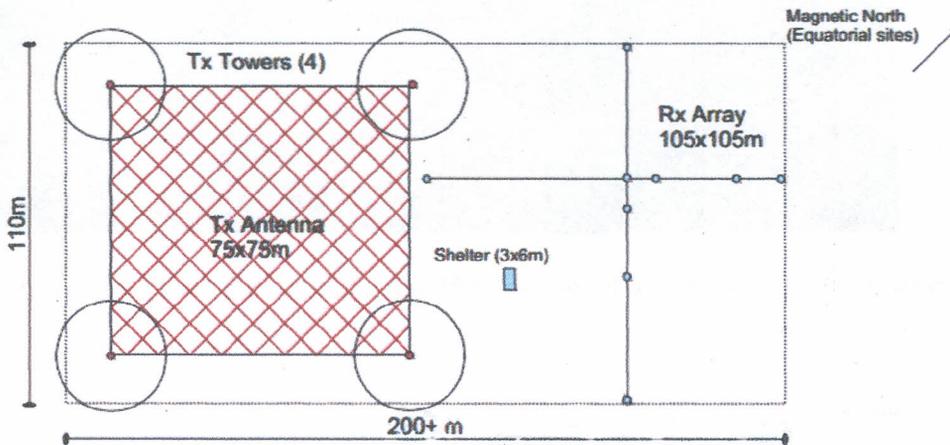
Figure 4: Architectural plan of a VIPIR site with the netted square showing the position of the log-periodic transmitter antenna to the left, the shelter at the centre, and the receiver antenna array to the right

The physical set-up of this system requires diverse specifications of antenna towers and RF cables, which varies from site to site depending on local conditions and on scientific goals.

23

The design in Figure 4 was thus selected for Puerto Maldonado due to its high resolution, reliability, and agile performance required for ionospheric research at the equatorial trough (Bullet, 2013). Figure 5 shows the actual site with four 35 m long steel towers (red and white), supported by guy wires, bearing a log-periodic transmitter antenna and eight receiver Rx array two of which can be seen at the background.
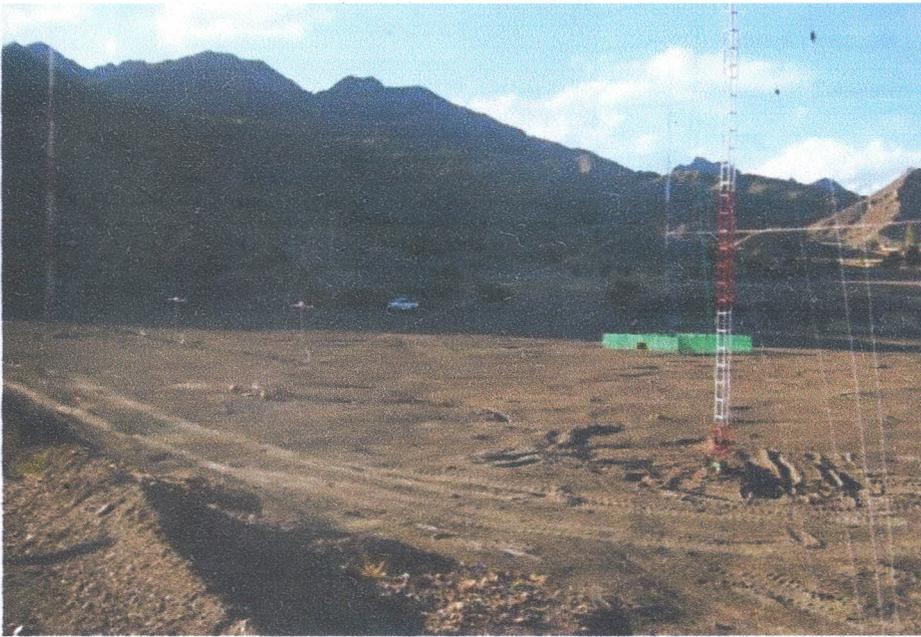

Figure 5: The VIPIR field site showing the 35m-long steel towers bearing the transmitter antenna strongly laterally supported by guy wires.

Figure 6 then shows the system rack comprising of six VIPIR modules (exciter, reference, receiver, front end, balun and a 4kW RF amplifier - TOMCO), a control and an analysis computer housed inside a 3 x 6m shelter seen in Figure 4.

24

Power Conditioner

4 kW RF Amplifier (Transmitter)

Keyboard Video Mouse (KMV) Switch

Exciter

Reference

Receiver

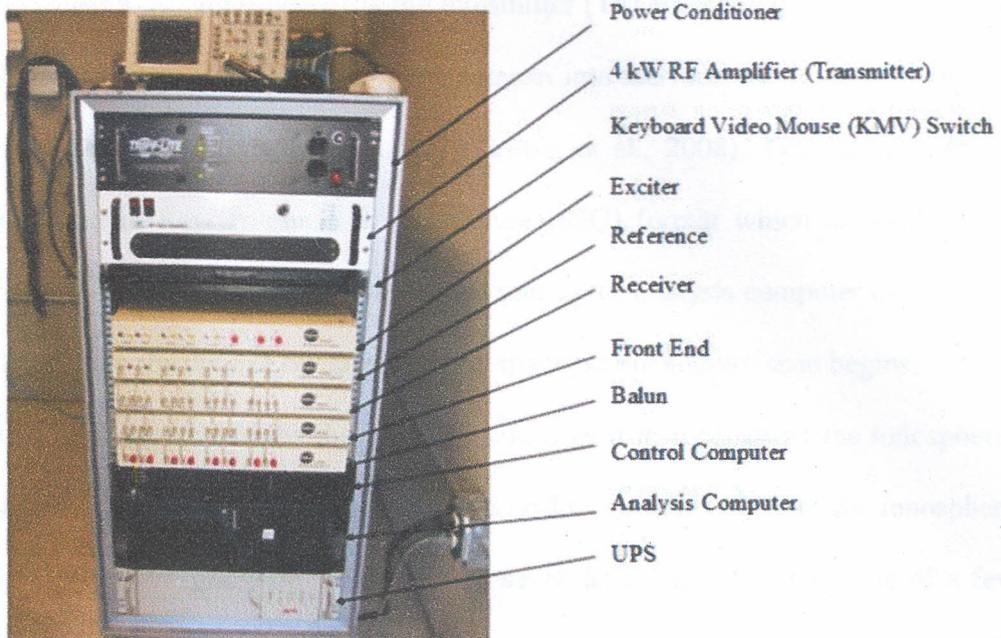Front End

Balun

Control Computer

Analysis Computer

UPS

Figure 6: The system rack showing VIPIR modules (exciter, reference, receiver, front end, balun and a 4kW RF amplifier - TOMCO), UPS, a control and an analysis computer housed inside the shelter

A mains power conditioner and a UPS ensures a steady supply of power to these modules and computers, while a pulsed radio frequency (RF) amplifier generates the output for the transmitted scan. The analysis and the control computers both run on Linux operating systems (Debian) and use scripts for high level data collection and processing. The radar modules are interconnected using universal serial bus (USB) cables. More information about the VIPIR modules, connections and installation of this ionosonde can be freely obtained from National Oceanic and Atmospheric Administration (NOAA) website, (NOAA, 2013).

Once the connections are complete, the system is then started. The desired run mode (either dg21 or fast weep, depending on resolution and speed of scan) and the scan frequency is set. The RF power light on the TOMCO amplifier front panel blinks to verify that a scan is in progress while the control computer displays the scan status. During this period, an amplified HF

radio wave is propagated to the ionosphere via the transmitter (Tx) antenna and is received upon reflection from the ionosphere by the receiver (Rx) antenna into the receiver module, converted to digital signal and sent to the control computer (Grubb, et al., 2008). This computer then records this information in Raw In-phase & Quadrature (RIQ) format which is hundreds of megabytes in size (Grubb, et al., 2008). The file is then sent to the analysis computer over a local area network, deleted from the control computer to free space before another scan begins.

The analysis computer interprets the raw RIQ and uses it to reconstruct the ionospheric electron density profile. The output is then plotted on a grid of altitude/height of the ionosphere against frequency forming an ionogram which is then saved as an image (*.png) file of a few kilobytes. The time between signal transmission and its reception is used to establish the altitude of the ionosphere using the usual echo method (Emerson, 1998). However, assuming a constant speed of the radio wave in the ionosphere, only an apparent or virtual height (h'F) of the reflection can be calculated. A conversion procedure is required to determine the true or physical height of the signal reflection (e.g., Davies, 1980). In VIPIR system, a Polan program is used for this purpose (Titheridge, 1988). The analysis computer then avails the ionograms in real time to the internet over a wide area network (WAN). This data can then be downloaded from the LISN database and interpreted to reveal the behaviour and other features of the ionosphere above Puerto Maldonado.

The ionogram comprises of both ordinary, O and extra-ordinary, X-traces. The O-trace results from the acceleration of free electrons parallel to the magnetic field by the electric field of the incident radio wave while X-trace emerges when the electric field accelerates free electrons perpendicular to the magnetic field (Emerson, 1998). Therefore, there is force imposed on charged particles due to magnetic field for X-trace and none for O-trace. This signal polarization

26

causes a difference in the refractive index and results in different group velocities. The O-trace is thus considered in this study because it depends only on the local plasma frequency. Figure 7 shows an ionogram from this VIPIR station showing both the O-trace (red) and the X-trace (green) electron density profiles at 10:03 universal time (UT) for 24th July 2011.
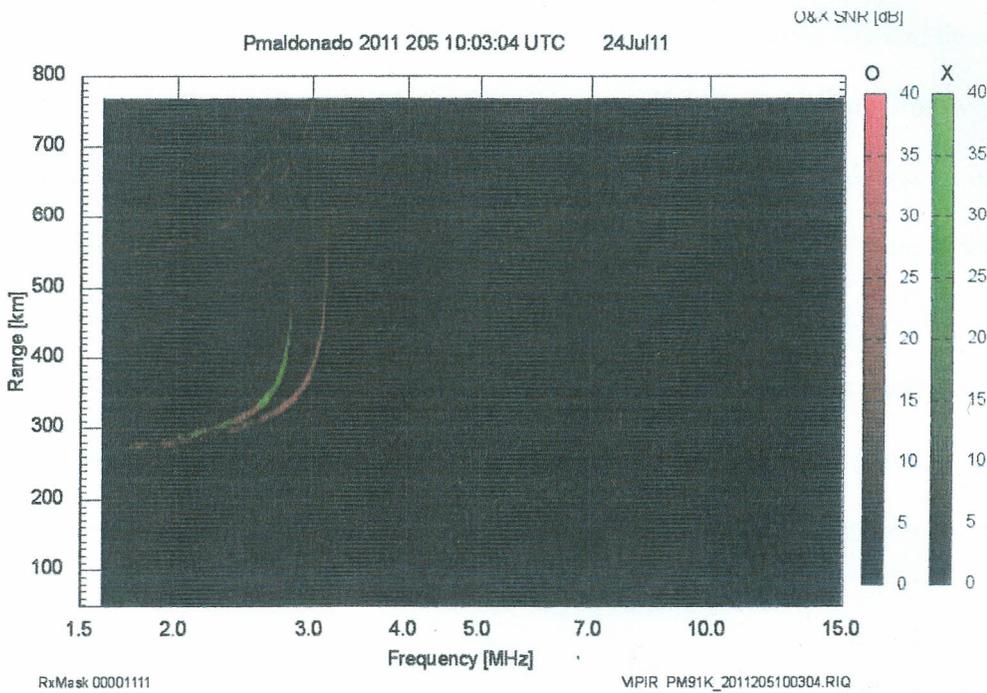

Figure 7: A typical ionogram from VIPIR ionosonde showing a clear distinction between the O-trace and the X-trace.

3.2 Data Rationale and Processing

The run mode for the ionosonde was set at dg21 which offers high resolution and the time interval for scanning set at 15 minutes bearing in mind that the F-region electron lifetime is only 20 minutes (Bhattacharya & Pandit, 2014). The dg21 mode also ensures a clear distinction between the O and the X-trace to eliminate any confusion. The 15 minute periodic scanning produced four ionograms every hour and therefore 96 ionograms were collected everyday for a period of one year (December, 2012 to November, 2013). This period offered a good time to

observe the effects of solar flux on the dynamics of the F-region irregularities because of its unique epoch on the 24th solar cycle (April 2003 – April 2014) (Clette, 2015). During this period, the ascending arm of this solar cycle approached a maximum in April 2014 and the solar flux and its influence was expected to be well pronounced (Clette, 2015).

The virtual height at 4 MHz frequency was chosen due to the fact that at this low frequency, the transmitted radio pulses suffer very little delays in the ionosphere and thus causes not much difference between virtual and true height (Rao, et al., 2006). It is from this height that the vertical $\mathbf{E} \times \mathbf{B}$ drift is evaluated. The critical plasma frequency (foF2), which is an indicator of ionospheric plasma density, was also determined from every ionogram. Figure 8 shows an example of an ionogram from Kisumu, Kenya station showing critical frequency, foF2 = 13.14 MHz and the virtual height at 4 MHz sounding frequency, h'F = 285.13 km as indicated by the dotted vertical and the horizontal lines respectively. A similar approach was considered in this study for processing of the ionograms and a Matlab script was developed to help with the large data.
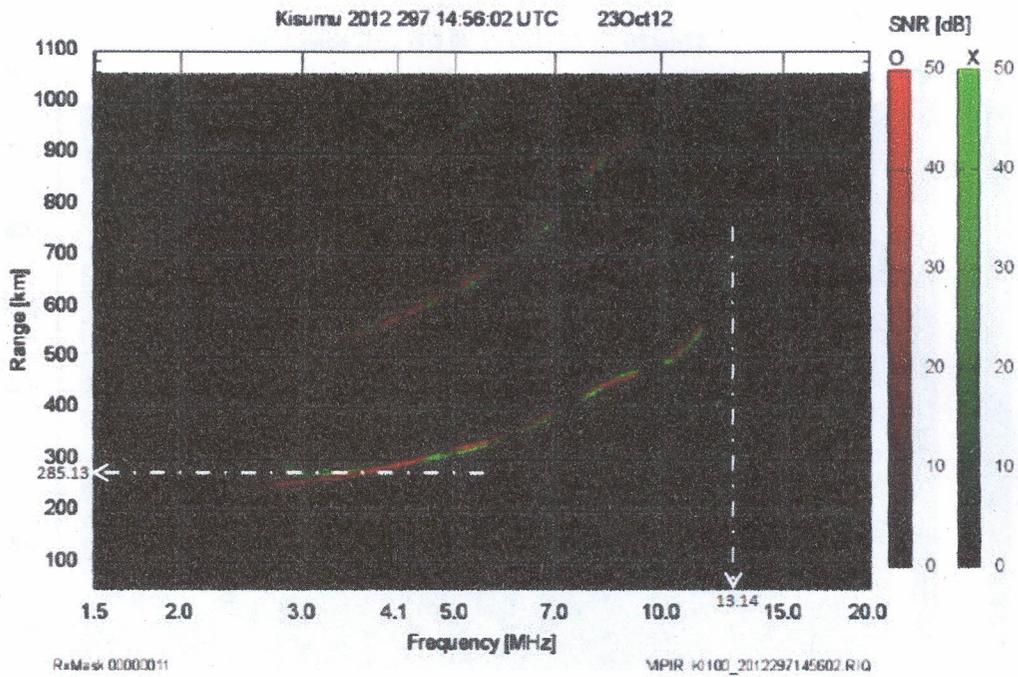
Figure 8: An ionogram sample from Kisumu –Maseno ionosonde station showing the critical frequency (foF2 = 13.14 MHz) and the virtual height (h'F = 285.13 km)

The daily 96 ionograms obtained in 15 minutes cadence were then manually scanned for spread F and the spread range estimates. Figure 9 shows a typical spread-F event of spread range 230 km occurring at about 2332 LT in Puerto Maldonado measured at 4 MHz frequency. Note local time (LT) in this location is 5 hours less its universal time (UT) and therefore 0432 UT is the exact equivalence of 2332 LT.
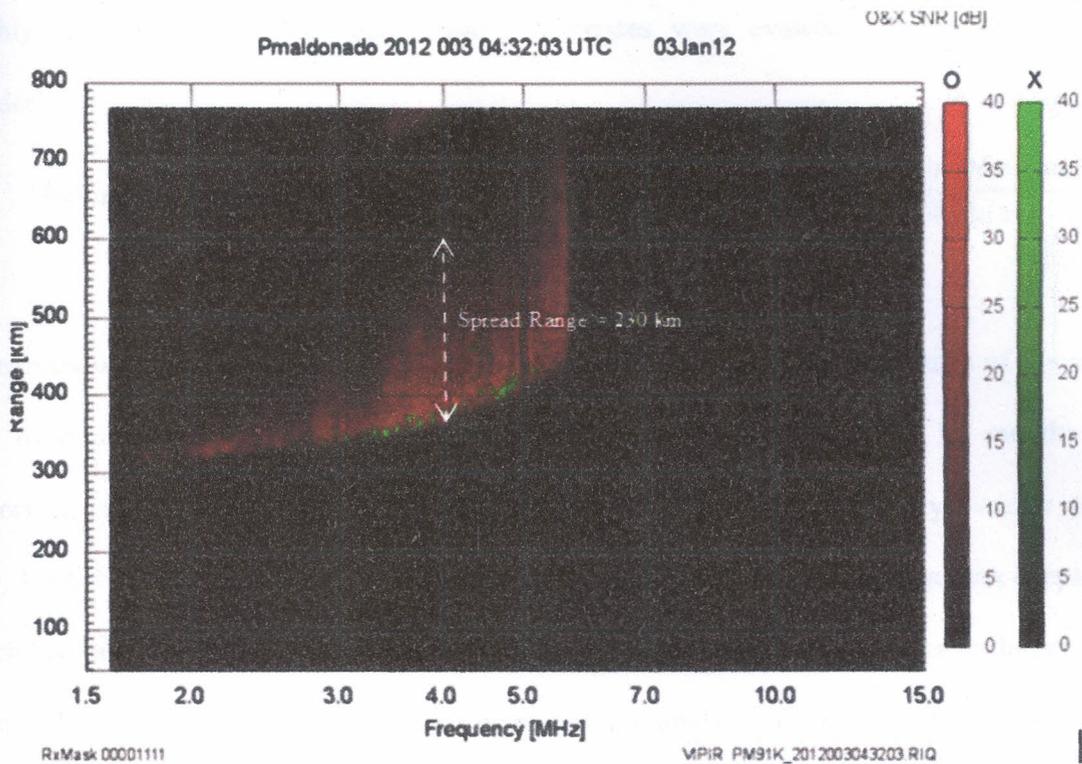
Figure 9: A spread-F event observed on 3rd January 2012 over Puerto Maldonado showing a

spread range of 230 km

3.3 Measurement Procedures

3.3.1 ESF Percentage Occurrence, Persistence and Intensity

All the daily ionograms recorded at 15 minutes cadence were inspected for F-region
spreading and the observed spreads were further categorized into pre-MN (1900 LT – 2400 LT)
and post-MN (2400 LT – 0800 LT) occurrences for all the days of the month. It was thus
possible to obtain the number of days with/without pre-MN occurrence and those with/without
post-MN occurrence. The monthly percentage occurrence of ESF was then evaluated by
considering the number of days with ESF events against the total number of days of the month to
evaluate the percentage occurrence pre-MN and post-MN periods. Equation 6 shows how the

30

monthly pre-MN or post-MN percentage occurrences were evaluated from the ionograms recorded.

$$\text{Monthly (preMN/postMN)\%age} = \frac{\text{Number of Days with preMN/postMN spread}}{\text{Total number of Days with data}} \times 100$$

.... 6

An analysis was carried out on the ESF percentage occurrence for all the months of the year in order to establish ESF seasonal variability over Puerto Maldonado. The 12 months were categorized into summer months (November, December, January, & February), winter months (May, June, July, & August), summer equinox (March & April), and winter equinox (September & October) as was done by Chen, et al., (2004). Summer solstice (December & January) and winter solstice (June & July) were also extracted for analysis from the summer and winter months respectively.

The daily pre-MN and post-MN occurrence durations/persistence were obtained from the time difference between ESF start-times and their end-times. The monthly-averaged start times and end times were obtained. The durations were then calculated and plotted against corresponding months to obtain the seasonal persistence trend. The start times were also recorded to provide information on the onset times.

The spread ranges for every ionogram with a spreading trace were measured as described in Figure 9 and then averaged (hourly then daily) to obtain the average daily spread range for the entire night. They monthly pre-MN and post-MN average spread ranges were then obtained from the daily and hourly averages. The daily average spread ranges were later plotted juxtaposed with daily solar flux values for the entire year to reveal possible influences of F10.7 on the seasonal variations of ESF intensity. The monthly averages for both pre- and post-MN spread ranges were also plotted against monthly averaged solar flux values to show any correlation.

31

3.3.2 Vertical E x B Drift

Unlike other studies (e.g. Rao, et al., 2006) who only settled for the highest drift velocity preceding a post-sunset ESF onset, the instantaneous vertical $E \times B$ drifts velocities V_t for this study were calculated by considering the rate of change in the vertical displacement of virtual height h'F at the 4MHz frequency trace after every 15 minutes of the day and for the entire year. This approach would help reveal any hidden behaviours of the drift that can influence the seasonal ESF variability and morphology. The upward (enhancement) drift and the downward (reversal) drift values were obtained from every two successive ionograms. Equation 7 shows a displacement equation, similar to that used by Dabas, et al, (2007), showing how the vertical drifts V_t were obtained:

$$V_t = \frac{dh'F2}{dt} \dotfill 7$$

where $dh'F2$ is the change in virtual height in meters and dt is the difference in time in seconds between two successive ionograms. A scatter-plot was then developed from the drift values to show the diurnal and seasonal variability of the drift and the plot was analyzed against diurnal and seasonal ESF occurrence to find any possibility of enhancing predictability. This was in light with the conclusion of Dabas, et al., (2007) that at or near the magnetic equator (not in higher latitudes), an upward enhancement in $E \times B$ drift to some threshold value is 90% sufficient for generation of ESF.

3.3.3 F10.7 and foF2

The solar flux values (F10.7) obtained from the Madrigal Database at Haystack Observatory (http://madrigal.haystack.mit.edu/madrigal/) which stores all solar flux information obtained from both in-situ and ground-based observations. The eight daily three-hour cadence of solar flux values in $10^{-22}Wm^{-2}Hz^{-1}$ were then averaged to obtain the daily averages for F10.7.

32

This was then plotted juxtaposed to the daily spread range values to find out trends that may help in explaining seasonal ESF behaviour. The daily averaged F10.7 values were further averaged to obtain monthly values for solar flux which was then analyzed against the total monthly averages of ESF percentage occurrence to find a correlation. Monthly averages of ESF occurrence were obtained by averaging the pre-MN and the corresponding post-MN spread occurrence percentages. The same treatment was done with the monthly average spread ranges to show proof of any relationship between spread intensity and solar flux.

As already discussed in the previous chapters, plasma critical frequency values were taken to represent the electron density as asserted by Buchert, (2007). The critical frequencies were extracted from every ionogram and recorded for the entire year of study. A scatter-plot was then generated from these values to show the diurnal and seasonal variability of the electron density. This plot was then analyzed as in the case of drift to establish any influence it has on ESF variability.

CHAPTER FOUR

RESULTS

4.1 Results for ESF Percentage Occurrence, Onset Times and Persistence

The monthly ESF percentage of occurrences for both pre-MN and post-MN periods were evaluated using Equation 6 as described in the preceding chapter and the obtained values were recorded. Table 2 therefore shows monthly pre-MN and post-MN percentage occurrences recorded between December 2012 and November 2013 over Puerto Maldonado.

Table 2: Monthly pre-MN and post-MN percentage occurrences over Puerto Maldonado between December 2012 and November 2013

The Average Monthly ESF Percentage Occurrence												
	Dec	Jan	Feb	Mar	Apr	May	Jun	Jul	Aug	Sep	Oct	Nov
Pre-MN (%)	92.86	96.67	89.29	77.42	55.56	5.26	23.33	27.59	19.35	40.00	54.84	77.78
Post-MN (%)	92.86	93.33	71.43	67.78	77.78	–	23.33	20.69	16.13	30.00	51.61	66.67

These values of percentage occurrences were then plotted against the corresponding months to show the spread occurrence trend and its seasonal variability over this equatorial station. Figure 10 is a two-curve plot displaying ESF monthly percentage occurrence and variability for both pre-MN and post-MN periods between December 2012 and November 2013. The figure shows a seasonal pattern of spread occurrence during the period of study.
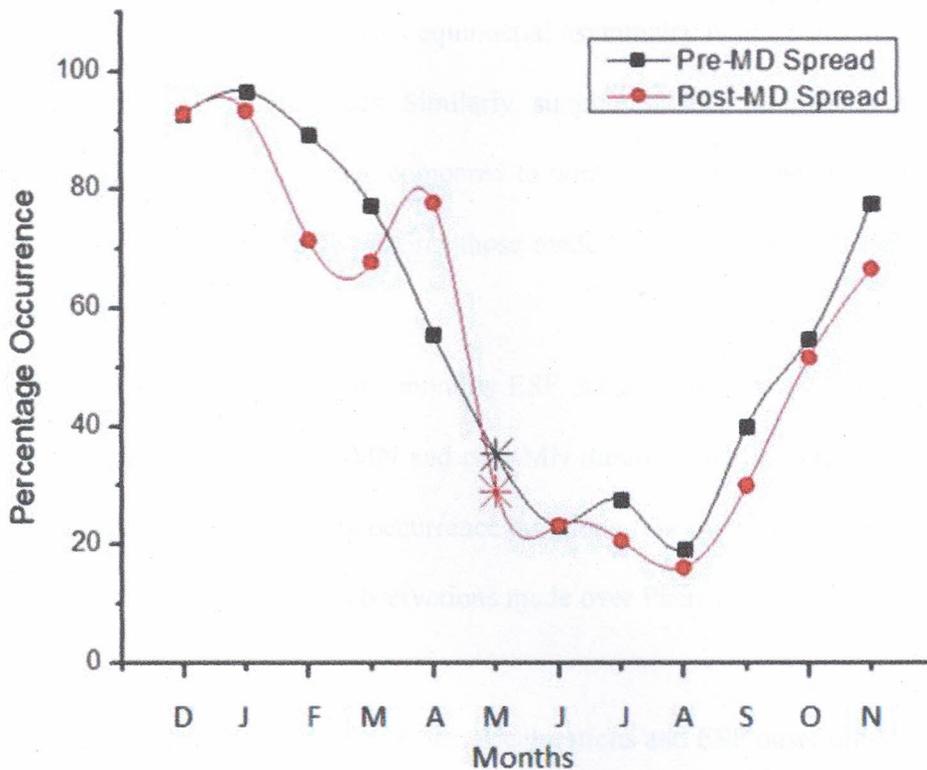
Figure 10: Seasonal monthly ESF percentage occurrence variation for both pre-MN and post-MN

ESF recorded over Puerto Maldonado.

It is remarkable to note that throughout the period of this study, ESF percentage occurrence trends measured for both pre-MN and post-MN periods followed a similar sequence as depicted in Figure 10. It indicates that both pre-MN and post-MN events had high occurrences of about 80-100% during the summer months (November, December, January, & February), and a minimum of about 25% during the winter months (May, June, July, & August). Pre-MN occurrence displayed a smoother trend in summer months than in wintertime while the post-MN occurrence had the most varied trend. It was also noted from Table 2 that summer equinox (March & April) generally registered a higher probability of ESF occurrence compared to winter equinox (September & October) and this is comparable to observations made by Su, et al., (2008) who correlated spread F occurrence probabilities with vertical plasma drift velocities and

35

noticed this occurrence asymmetry. This equinoctial asymmetry is more pronounced during the post-MN than in pre-MN occurrences. Similarly, summer solstice (December & January) had higher percentages of ESF occurrence compared to winter solstice (June & July) as depicted in Figure 10. These observations also confirm those made between April, 1999 and March, 2000 over Jicamarca by Chen, et al., (2004).

Table 3 then shows the average monthly ESF occurrence durations and ESF onset times obtained and recorded for both pre-MN and post-MN durations while Figure 11 is a two-curve plot displaying ESF average monthly occurrence durations. They both show the variability in the persistence and onset times of ESF observations made over Puerto Maldonado during the period of study.

Table 3: Average monthly ESF occurrence durations and ESF onset times recorded for both pre-MN and post-MN durations

| Monthly Averages of Onset times and Duration of Spread				
	Pre-MN		Post-MN	
	Start time (LT)	Duration (hrs.)	Start time (LT)	Duration (hrs.)
Dec	1829	7.47	0134	2.87
Jan	1914	7.00	0154	2.42
Feb	1853	6.83	0215	2.12
Mar	1822	7.15	0226	2.10
Apr	2155	4.05	0237	2.43
May	2022	2.25	-	3.01
Jun	2313	2.00	0222	3.75
Jul	2152	3.10	0028	5.03
Aug	2035	4.22	0007	5.50
Sep	1949	4.75	0143	2.55
Oct	1904	6.17	0200	2.52
Nov	1956	4.78	0100	3.43
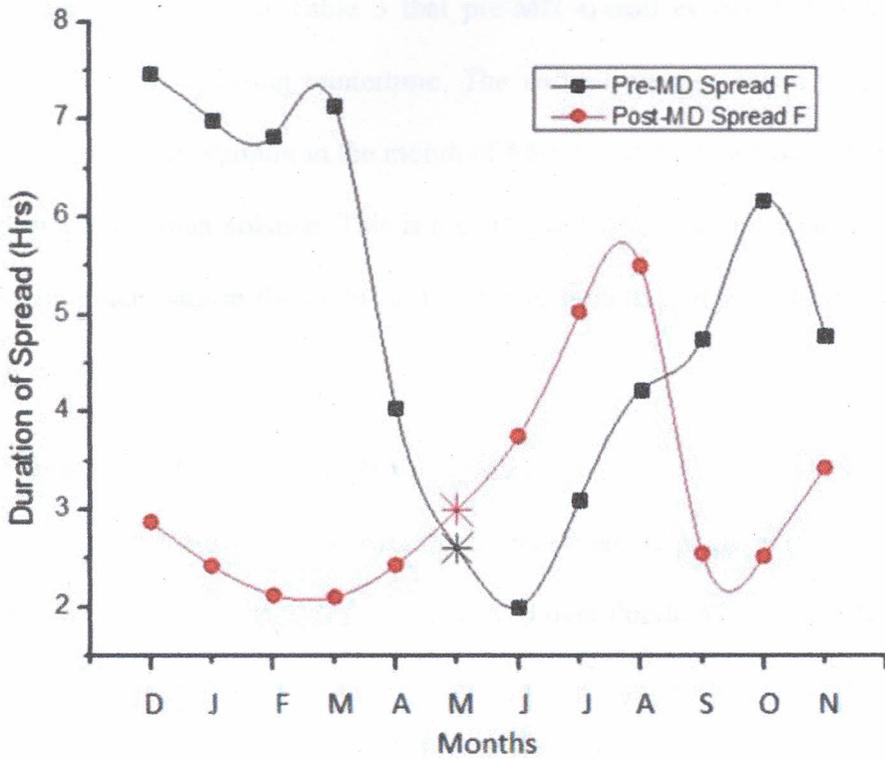
Figure 11: Annual persistence trend for both pre-MN and post-MN ESF recorded over Puerto Maldonado

From Figure 11, it was observed that pre-MN ESF events registered longest duration of occurrence of about 7 hours averaged for summer months compared to values of about 4-2 hours recorded for winter months. This resonates well with the observed ESF occurrence trend in Figure 10. However, in a twist of trend, it was noted from Figure 10 and 11 that, months with highest percentage occurrence and longest duration of pre-midnight ESF registered the shortest post-midnight spread F occurrence durations. In essence, the durations of pre-MN events were significantly longer (~7 hours) in summer months (November, December, January, & February) compared to the durations (~2-4 hours) observed during the rest of the year. However, the post-MN ESF always lasted about 1-2 hours longer in winter months than in summer months (3-5 hours versus 2 hours), which is a very unique observation.

37

It is also noticed from Table 3 that pre-MN spread events commenced much earlier during summertime than during wintertime. The earliest average onset time at 1822 LT was recorded during summer equinox in the month of March and the latest onset happened in June at 2313 LT during the winter solstice. This is a significant difference of about 5 hours and implies that ESF starts much later in the night during winter months and persists towards dawn than in the summer months.

4.2 Diurnal and Seasonal Drift Variability

Figure 12 is a scatter-plot showing the diurnal (vertical axis), annual variability (abscissa axis), and the vertical plasma drift (colour) observed over Puerto Maldonado during the period of study.
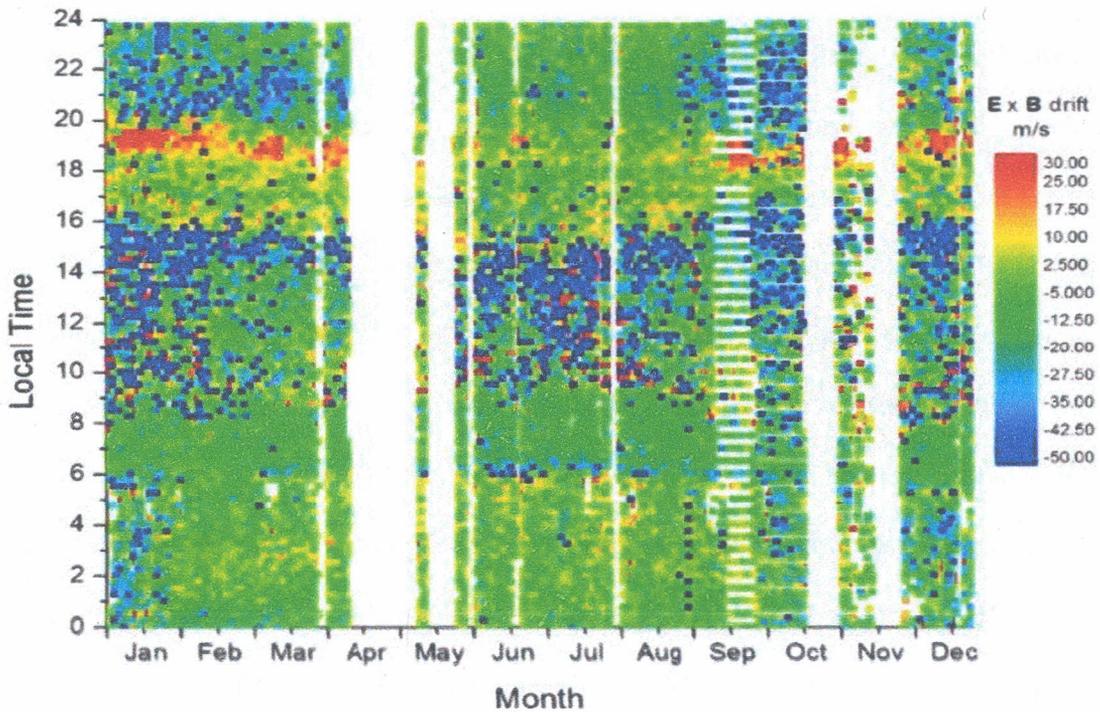
Figure 12: The diurnal and seasonal variability of **E** x **B** drift over Puerto Maldonado displaying unique diurnal phases.

38

From Figure 12, it can be observed that the **E** x **B** drift velocity enhancements over Puerto Maldonado displays unique diurnal and seasonal variability. Diurnally, it is clear from the figure that the vertical drift displays local time dependence. During 0600-0800 LT, the morning bottomside seem to be relatively stable throughout the year. The daytime drifts(0800-1600 LT) are however an irregular combination of upward enhancement and downward reversal with the equinoctial months experiencing extremities of about 25 m/s and −50 m/s. It is also notable that this phase lasts for longer hours in summer solstice (0700-1600 LT) than in winter solstice (0900-1500 LT) and is most intense during equinoctial months.

The third phase (1600-1900 LT) is the pre-reversal enhancement (PRE) phase shown by the red band in Figure 12 with initial velocities of about 10 m/s which then shoots to a maximum of about 30 m/s at around 1800-1900 LT depending on the season. While its initiation velocity at 1600-1700 LT remains uniform throughout the year, the PRE attains a peak and final velocity between 1800 and 1900 LT and it exudes seasonal dependence similar to what was observed by Chapagain, (2011) and Chen, et al., (2004) over Jicamarca during post-sunset hours. The drift is strongest in summer months, but weakest in winter months as shown in Figure 12. Nevertheless, maximum PRE is attained about 1 hour later in summer months than in winter months as was also confirmed by Chen, et al., (2004). It exhibits a very close correlation to the occurrence and persistence of ESF as shown in Figures 10 and 11 respectively. This phase lasts longest but is weaker in winter solstice than in summer solstice thus exuding a solsticial asymmetry. However, the PRE shows an equinoctial symmetry (same magnitude and start time) contrary to what has been observed for ESF occurrence in Figure 10.

The nighttime phase (2000-0600 LT) is the longest phase that characterizes the diurnal drift with the F layer generally experiencing a reversal drift to about -30m/s after around 2000

39

LT. During summer solstice and in equinoctial periods, a sharp reversal begins shortly after 1900 LT. However, the wintertime do not experience very steep nighttime reversal drifts.

4.3 Solar Flux and Spread Range

Figure 13 displays daily averages of F10.7 values and the corresponding average spread ranges plotted juxtaposed on a double-graph to show the influence of solar flux on the intensity of spread for the entire period of study.
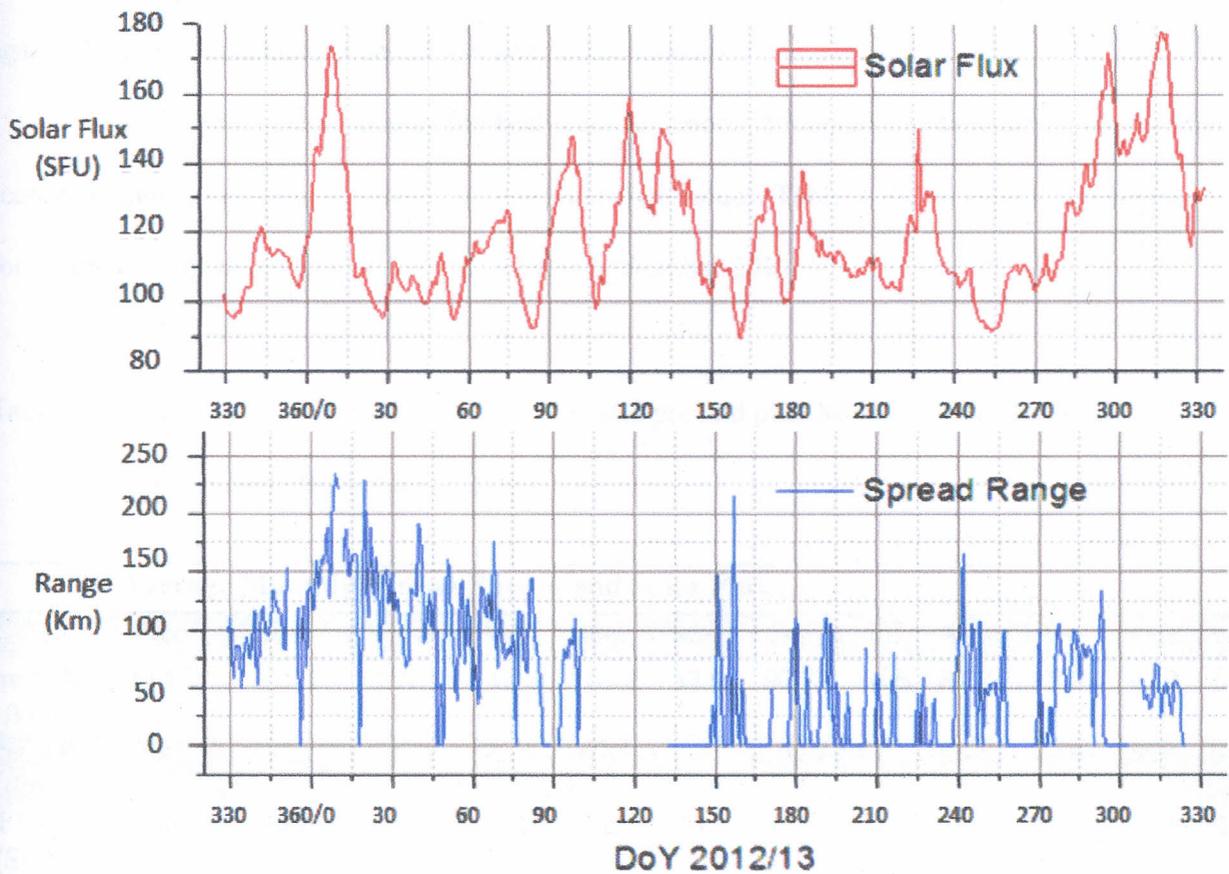

Figure 13: Solar flux (upper plot) and ESF range (lower plot) variability for the one year period juxtaposed to show possible dependence

It shows the annual behaviour of ESF ranges and the solar flux variation showing the high peaks of spread ranges matching with low peaked F10.7 values and vice-versa. This

generally indicates that increase in solar flux inhibit the strength of ESF over Puerto Maldonado. Except for the first half of January where high solar flux index (>170 SFU) corresponds to a very long spread range (>225 km), the remaining periods of summer solstice and summer equinox generally exhibit high spread ranges (>150 km) against extremely low solar flux indices (<100 SFU). The month of November, for example registered solar flux values greater than 170 SFU corresponding to spread ranges of below 50 km. As observed, the days of winter solstice and winter equinox displayed generally moderate and low solar flux indices respectively matching against low and moderate ranges of spread in these months.

The monthly spread ranges for both pre- and post-MN epochs were then obtained and recorded against the corresponding average solar flux values. Table 4 shows the results obtained for all the months between December 2012 and November 2013.

Table 4: The average monthly solar flux in SFU and pre and post-MN ESF spread ranges recorded over Puerto Maldonado

The Average Monthly Spread Ranges and Solar Flux												
	Dec	Jan	Feb	Mar	Apr	May	Jun	Jul	Aug	Sep	Oct	Nov
Pre-MN (km)	114.2	180.1	137.1	110.3	103.8	53.0	92.3	56.6	88.2	85.9	97.3	54.1
Post-MN (km)	79.7	121.6	66.7	75.6	67.1	-	110.7	88.2	66.8	48.4	54.4	38.0
F10.7 (SFU)	108	127	104	111	125	131	110	115	115	103	132	148

Generally, the summer months recorded very long spread ranges compared to winter months as depicted in Table 4 and Figure 13. However, Table 14 further reveals that pre-MN spread ranges were always longer than the post-MN values except for June solstice. This high

41

post-MN ESF intensity noted during the month of June confirms earlier observations by Yizengaw, et al., (2013).

The data in Table 4 was then plotted to obtain correlations between solar flux and spread ranges (ESF intensity). A further correlation was carried out using data from Table 2 to reveal the dependence of both pre- and post-ESF percentage occurrence on solar flux. Figure 14 therefore shows the monthly averages for both pre- and post-ESF spread ranges plotted against corresponding values of solar flux, while Figure 15 is the correlation of ESF occurrence and solar flux.
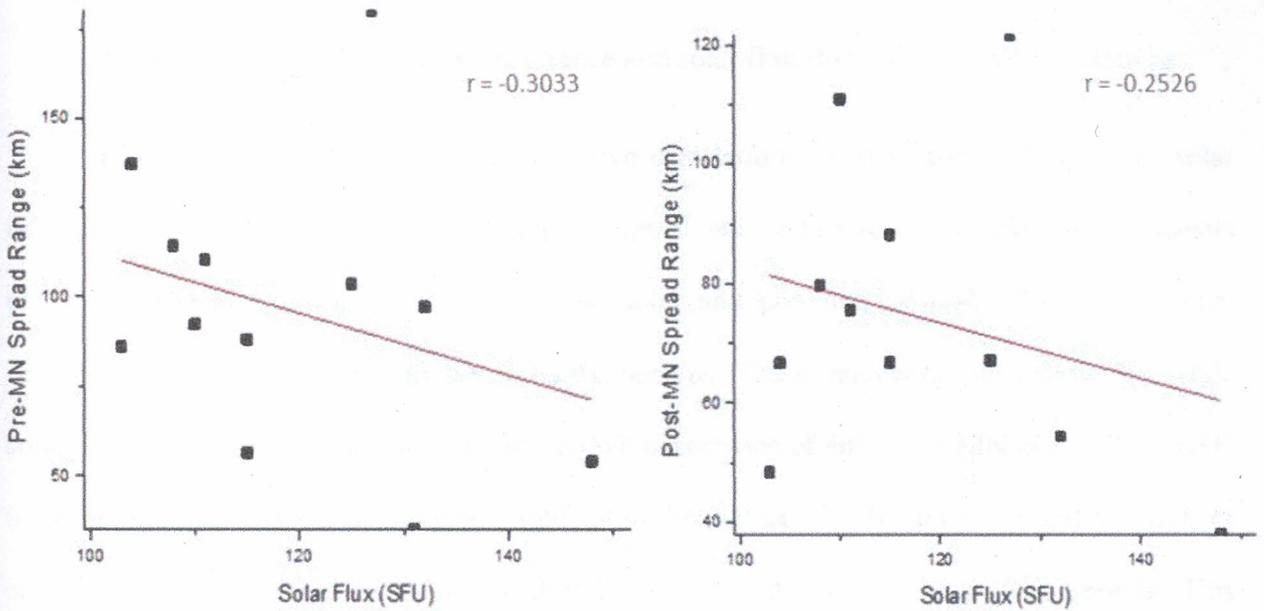

Figure 14: Pre- and post-ESF spread range and solar flux showing correlations
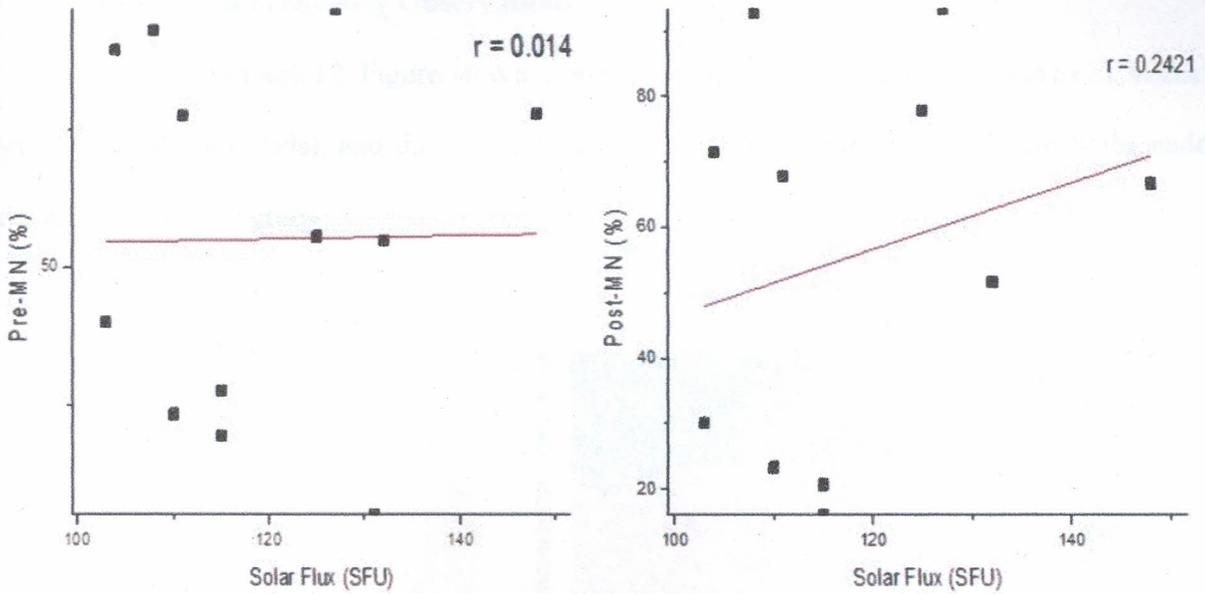
Figure 15: Pre- and post-ESF occurrence and solar flux showing positive correlations

From Figure 14 we notice weak negative correlations of -0.30 and -0.25 between solar flux and the pre- and post-MN spread ranges respectively. In Figure 15, correlation coefficients of 0.01 and 0.24 were also noticed between solar and pre- and post-MN ESF occurrences respectively, depicting very weak positive relationships. These interesting plots show that while solar flux has negligible positive influence on the occurrence of either pre-MN or post-MN ESF, increase in solar flux seems to have slight inhibition effect on ESF intensity and strength of spreading. High ESF intensities would thus be expected during low solar flux periods. This inverse correlation between ESF intensity and solar flux in Figure 14 has also been reported by Oyekola and Oluwafemi, (2009) and Candido, et al. (2011) and further confirms the results of a global study carried out by Stolle, Luhr, and Fejer, (2008) using CHAMP satellite who also noted negative values of threshold drift during June solstice and equinoctial months for solar flux levels below 110 SFU.

43

4.4 Critical Frequency Observations

Similar to Figure 12, Figure 16 is a scatter-plot showing the diurnal (vertical axis), annual variability (abscissa axis), and the critical frequency (colour) recorded from Puerto Maldonado during the period of study.
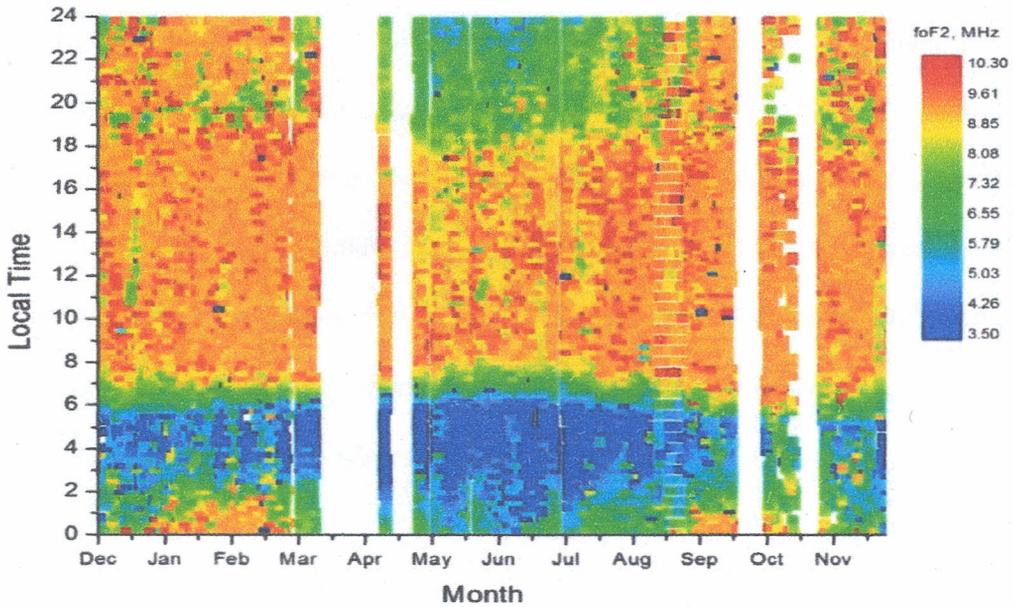

Figure 16: Diurnal and seasonal variation in the foF2 as a function of electron density over Puerto Maldonado

Generally, the figure shows that the daytime foF2 drastically increases from a minimum value of about 3MHz at 0500 LT to a high of about 9.5MHz at around 0800 LT before it steadies until 1700 LT. The steady daytime frequency is however slightly lower in winter months compared to higher values in summer months. The nighttime ionosphere experiences the greatest variability in electron density and portrays a similar trend to the ESF occurrence behaviour depicted in Figure 10. It decreases to a minimum value shortly before 0500 LT. However the

pre-MN values remained higher in summer-half year than in winter-half year showing a good correlation with the ESF occurrence pattern. The post-MN foF2 values also experienced a similar trend to the pre-midnight observations except for the fact equinoctial months exhibited high foF2 values for a duration of about 2 hours after midnight while winter solsticial periods experienced nights of intense electron density depletion and extremely low critical frequency values. It is also imperative to point out that the winter months registered very low plasma critical frequencies principally during the post-midnight periods. Although this study was conducted for a solar maximum, these foF2 observations are in agreement with the equatorial results reported over Cachoeira Paulista (Brazil) by Candido, et al., (2011) which showed that the lowest values of plasma critical frequencies is common during June solstice at solar minimum period. This is rather expected since in general, the ionospheric peak density climatology is known to show less variability compared to ESF phenomena (Zolesi, & Cander, 2014).

CHAPTER FIVE

DISCUSSION

5.1 Seasonal Variability of ESF over Puerto Maldonado

5.1.1 Pre- and Post-MN ESF Prevalence

It has been revealed in Figure 10 that the seasonal occurrence for both pre-MN and post-MN ESF over Puerto Maldonado generally experienced a similar trend of occurrence with the summer months (November, December, January, & February) having high occurrences of almost 80-100%, and a minimum of about 25% during winter times (May, June, July, & August). This pattern exhibits a very close correlation with the seasonal **E x B** plasma drift measured in this study (Figure 12). According to Abdu, (2012), the low PRE drift velocities that characterize the winter months (~10m/s observed for this study) slows down the rate of post-sunset plasma instability growth normally initiated by gravity wave seed perturbation and has the implication of longer time needed by the ESF to spread and evolve to the F-region topside. However, during summertime, the drifts increase considerably to ~30m/s as observed in this study thus quickening the rate of instability growth to the topside. This explains why winter times registered lower pre- and post-MN ESF occurrence probability than summer months. A similar seasonal trend had been reported by Fejer, Scherliess, and de Paula, (1999), Chen, et al., (2004), and Chapagain, (2011) who also found a close correlation between ESF occurrence and the large upward **E x B** drift observed over Jicamarca.

Generally, the equinoctial epochs recorded asymmetrical prevalence with the summer equinox having a higher occurrence than the winter equinox. This high rate of ESF occurrence is attributed to large upward drifts that lift the F-region to higher altitudes creating favorable conditions for RT instability while larger eastward **E**-field leads to drift instability during winter

46

(Chen, et al., 2004). However, this equinoctial ESF prevalence asymmetry seems to occur regardless of symmetrical drift behaviour observed in Figure 12 implying that factors other than the vertical plasma drift could be responsible. Furthermore, it is more pronounced in post-MN occurrence than in pre-MN times. According to Stolle, et al., (2008), this difference in equinoctial ESF prevalence can be attributed to difference in plasma distribution carried on from the preceding solstice season. They further argue that high electron density and increased F-region irregularities during summertime enhances the electron density and ESF occurrence in the summer equinox while a highly depleted winter F-region influences the dynamics of winter equinox. Elsewhere, a study done by Manju, et al., (2012) attributes this equinoctial asymmetry to the effects of neutral wind dynamics which inhibits ESF initiation during winter and equally enhances it during the summer equinox when the meridional winds are stronger.

Summer solstice showed a vastly superior (about 5 times greater) ESF prevalence compared to June solstice, a phenomenon essentially explained using gravity wave-**B**-alignment (GWBA) theory (Tsunoda, 2010 and Paznukhov, 2011). According to this theory, the Inter-Tropical Convergence Zone (ITCZ) plays a major role in the development of gravity waves which is presumed to be a major trigger mechanism for ESF generation. At the ITCZ, the northward and southward planetary winds and pressure systems meet pushing the air mass upwards. This causes gravity waves which enhances the vertical plasma drift by propelling the F-region to greater heights. The ITCZ keeps migrating with seasons and in the South American sector, its mean position is closest to the geomagnetic equator in December and furthest in June (Tsunoda, 2010). The gravity waves are thus strongest in December and weakest in June hence causing ionospheric uplifting (i.e., vertical plasma drift) during the solstices as shown in Figure

47

12. This further explains the ESF prevalence asymmetry observed in Figure 10 during summer solstice and winter solstice.

5.1.2 ESF Onset Times and Persistence and Intensity of ESF

From Figure 11 and Table 3, the onset times and durations of ESF events were distinctively different for the pre-MN and post-MN epochs with the pre-MN ESF events registering longest periods of occurrence of about ~7 hours averaged for summer months compared to values of about ~3 hours recorded for winter months. On the contrary, the average duration for post-MN ESF was always about 1-2 hours longer than the pre-MN occurrence durations (3-5 hours versus ~2 hours) during winter months. The pre-MN spread-F irregularity during summer months is triggered by the early steepening of the bottom side post-sunset F-region emanating from increased recombination and electro-dynamical effects (Somoye, 2010). Sudden strong post-sunset PRE causes rapid rising of the equatorial post-sunset F-layer and plays a significant role in the early ESF initiation process in summertime. This explains why seasons with high ESF prevalence registered equally high pre-midnight ESF persistence but very low post-midnight ESF duration of occurrence. Yizengaw, et al., (2009) too while acknowledging PRE as one of the prime triggering agents of post-sunset ESF pointed out that sudden change in electric field direction from westwards to eastwards is the major cause of post-midnight irregularities during active solar conditions.

Conversely, during wintertime, the often weak post-sunset PRE takes a longer time to attain a threshold value or fails to attain it at all (as shown in Figure 12) and this explains the 5-hour maximum delay in ESF onset observed during June as compared to December. This elongated period of slow upward ascent seems to over-expose electrons to the meridional polarization drifts extending the lifetime of the few occurring spread events towards dawn

48

(Somoye, 2010). During the post-MN hours, this situation is further complicated by the post-midnight reversal of the zonal electric field from westward to eastward making the F-layer to descend under the effect of electric field drift (Rishbeth, 2000). This drift results in post-midnight ESF onset which may extend to longer periods of time depending on the strength of the initiating drift. This confirms the assertion by Sastri, (1983) that the duration/persistence of post-midnight ESF depends upon its initial strength. They further pointed out that, in the absence of other sustaining mechanisms after its initiation, ESF lifetime depends upon its initial strength and on the recombination rate (Sastri, 1983). Therefore, during winter months, the magnitude of plasma reversal enhancement is weaker causing the F-layer to rise slowly leading to longer post-midnight occurrence than in summertime as in Figure 11.

This further helps to explain the high intensity (large spread ranges) of ESF observed during summer months (Figure 13 and Table 4) and low ESF intensity during winter with an exception of the June solstice which recorded an abnormally high ESF intensity. This exception in June has also been reported by Yizengaw, et al., (2013) who concluded that the high ESF intensity is enhanced by the frequent appearance of sporadic E during June solstice causing eastward polarization in electric field resulting in quiet-time post-MN ESF.

5.2 Influence of Drivers on ESF Dynamics

Having discussed the possible physical mechanisms responsible for the observed seasonal and diurnal variation of ESF over Puerto Maldonado, this study further identifies the possible precursors, attributed to vertical plasma drift, solar flux variation, and ionospheric critical frequency, which would influence the initiation and evolution of ESF over the dip equatorial region of Puerto Maldonado.

49

5.2.1 Vertical E x B Drift Influence on ESF

From Figure 12, morning hours experience a completely reversed (eastward) zonal electric field marking the end of a purely downward drift and commencing the upward lift of the F-region (Risbeth, 2000). This bring an end to the relatively quiet F-region bottomside witnessed between 0600 LT and 0800 LT in Puerto Maldonado. However, as the day progresses, the drifting of ionosphere becomes very irregular as witnessed between 0800 LT and 1600 LT with a mixed influence of both upward and downward drifts in what appears to be a consequence of some two major anti-parallel forces. Increase in photo-ionization seems to enhance plasma density thus driving the F- region generally downwards under the influence of a dominant gravitational drift against the upward drift generated by the zonal (eastward) electric field (Chen, et al., 2004). It is also notable that this phase lasts for longer hours in summer solstice (0700-1600 LT) than in winter solstice (0900-1500 LT) and is most intense during equinoctial months and could partly be the reason behind early onset of pre-MN ESF during summertime as already discussed.

The PRE drift then commences between 1600 LT and around 1900 LT when it attains a threshold vertical drift of ~30m/s. This phase lasts longer (but is weaker) in winter solstice than in summer solstice thus exuding a solsticial asymmetry. The results of this study show that ESF is more prevalent in summer and equinoctial months than in winter months correlating well to the strength of PRE. This reveals that PRE drift plays a major role in the seeding mechanism of ESF (Chen, et al 2004). The reduced PRE in winter months observed in this study were also witnessed by Su, et al., (2009) over the Peruvian longitudinal sector and they ascribed it to the ionospheric electro-dynamical effect emanating from the degree of alignment between the magnetic field line and the sunset terminator. Positive **B**-field declination angle provides a

50

favourable alignment condition and results in very high evening vertical drift and an early rise in the F layer height, increase in RT instability growth rate leading to early start time and high ESF prevalence during solar maximum. This is confirmed by the early drift and high ESF occurrence results observed in summertime during this study and is further validated by the gravity wave-**B**-alignment (GWBA) theory championed by Tsunoda, (2010). It has also been noted in this study that longer periods of PRE drift in winter months further increases the durations of post-MN ESF occurrence, a fact which can be explained by the increased time for meridional plasma diffusion along the magnetic field leading to increased post-MN spreading as observed in June (Rishbeth, 2000; Liu & Wan, 2001).

5.2.2 Critical Frequency (foF2) Implications

Summer months with the highest foF2 values implying high electron density (Figure 16) experienced the most intense spreading of the ionogram traces and the highest prevalence of ESF during both pre-MN and post-MN epochs. However, the wintertime is characterized by low foF2 signifying highly depleted ionospheric electron densities, low ESF prevalence, but high post-MN ESF durations. This summarizes the summer observations from Table 2 and Figure 16 that high electron densities during the post-sunset hours is a precursor to long ranges of F-spread and depicts high ESF prevalence as shown in Figure 11. The high daytime ionospheric electron density is further enhanced by the increased photo-ionization during summer months and equinoxes as depicted in Figure 16. However, the wintertime recorded highly depleted plasma density observations which agrees with the equatorial results reported over Cachoeira Paulista (Brazil) by Candido, et al., (2011) during June solar minimum. Therefore, very low ionospheric electron density is an indicator of retarded ESF development hence very short ranges as recorded in Table 2 for winter months. Low electron density during post-MN periods is due to a

combination of physical processes including increased recombination, reduced photo-ionization, and plasma diffusion along geomagnetic field lines by meridional plasma drift (Rishbeth, 2000; Liu & Wan, 2001; Zolesi & Cander, 2014).

5.2.3 Effect of Solar Radiation Flux on ESF prevalence and Intensity

The weak, but significant positive correlation reported between solar flux observations and the pre- and post-MN ESF percentage occurrence values (Figure 15) is in complete agreement with what has been extensively reported for low latitude regions (e.g. Stolle, et al., 2008; Chapagain, et al., 2009; Cueva, et al., 2013). Furthermore, the inverse correlation recorded in Figure 14 between solar flux and ESF spread range has also been observed by Oyekola and Oluwafemi, (2009) and Candido, et al., (2011). According to Candido, et al. (2011), the negative correlation between solar flux and ESF intensity results from the influences of Travelling Ionospheric Disturbances (TIDs) and/or extremely low plasma densities, however, the latter reason doesn't seem to hold for our study which was held on a solar maximum epoch when plasma densities were high.

Stolle, et al., (2008) further argued that when solar activity is low, the PRE vertical plasma drift becomes significantly weak and often downward drifts can occur. Therefore, since plasma density is also weak in winter months, some excursions to positive PRE drift values can still result in positive RT growth rates courtesy of low ion-neutral collisions frequency. This implies that ESF occurrence rates can still be above zero even during low solar months and in low plasma density conditions when nighttime post-PRE drift reverses.

In another study of the parameters influencing the evolution and inhibition of post-sunset plasma instability over Ouagadougou (dip lat. 3°N), Oyekola and Oluwafemi, (2009), like Chapagain, et al., (2009) noted that peak F-layer height and vertical plasma drift velocity

decrease significantly with the increase in solar flux during low solar activity periods a behaviour they argued was due to the effect of the meridional neutral wind on the vertical **E** x **B** drift and the nighttime peak F-layer resulting in diffusion and depletion of plasma. On the other hand, they observed no significant relationship during high solar activity (F10.7 > 200 SFU) and stated that the poor evolution of post-sunset plasma instabilities during high solar flux was due to the confinement of PRE drift peak and the F-layer peak to a narrow altitude range. This is however still subject to further research.

5.3 Comparison with other Studies

A comparison done on the findings of this study against those of some equatorial spread-F characterization studies carried out in the Indian (Trivandrum - dip lat. 8.2°N) and South American regions (Jicamarca - dip lat. 0.5°N) has exposed some unique similarities and differences. Sewing together these findings is not only fundamental to attaining global climatology of ESF, but also important in establishing the geophysical mechanisms responsible for these variations.

During the high solar activity year of 2001, Dabas, et al. (2007) while carrying out an ESF related study over Trivandrum, along the Indian equatorial crest revealed that summer (JFN&D) and equinoctial (MAS&O) months registered higher monthly percentages for both pre- and post-midnight ESF occurrences compared to winter (MJJ&A) months. This observation is in agreement with the results of the current study which further revealed the equinoctial and the solsticial asymmetry on ESF prevalence (as previously discussed). Their study showed that over Trivandrum, maximum ESF prevalences for summer and winter were about 83% and 30% respectively while this study reveals that there exists an almost similar trend with summer and winter months registering maximum ESF occurrences of about 100% and 25% respectively. The

pre-MN and post-MN ESF events both registered maximum occurrences of almost 100% during the summer half-year, and a minimum of about 20% during the rest of the year. The reason for this asymmetry is due to the influence of gravity waves and the migration of ITCZ as already discussed in the previous chapter.

This study further reveals that the threshold $E \times B$ drift for ESF development above the South American equatorial trough is almost double that of the Indian equatorial trough which is at 15m/s. Dabas, et al., (2007) further pointed out that the threshold $E \times B$ drift preceding ESF onsets increases with increase in altitude and the role of this drift in ESF prediction becomes less and less accurate with increase in latitude due to the effects of some other controlling factors like gravity waves, background electron density variations and the neutral winds.

Elsewhere in South America, a study carried out on the post-sunset ESF climatology over Jicamarca (dip lat. $0.5^{\circ}N$) with the aid of an Incoherent Scatter Radar revealed that the percentage of radar plumes observed above 900km during the equinoxes and summer months for a solar maximum was 75% (Chapagain, et al., 2009). The finding of this study however reveals a sharp asymmetry in the occurrence of ESF between March and September equinoxes. This skewness is further observed in the periods of summer and winter months as has been explained. Therefore, there exists a distinctive difference in the equinoctial observations made above Jicamarca and that over Puerto Maldonado. A study carried out on the Indian ionosphere by Manju, et al., (2012) has also established this equinoctial asymmetry and has attributed it to the role of neutral dynamics during the two equinoxes.

Over Jicamarca, another study done on the F-layer pre-reversal drift velocities and drift peaks preceding the onset of ESF portray both seasonal and solar cycle dependence (Chapagain, et al., 2012). They pointed out that ESF onset time has no dependence on solar flux, but depends

majorly on altitude, and that the observed percentage of radar plume remains at 25% during winter solstice, both for solar maximum and minimum (Chapagain, et al., 2012). Contrary to this observation, the current study however confirms the widely reported direct correlation between ESF occurrence and solar flux (e.g. Cueva, et al., 2013), but is in close agreement with the 25% ESF occurrence observed over Jicamarca during winter solstice.

Therefore, seasonality of ESF and the dynamics of its drivers have clearly confirmed the existence of major seasonal, latitudinal and longitudinal variations in ESF occurrence. A comparison of Puerto Maldonado observations to those from two other equatorial trough stations, Trivandrum (dip lat. 8.2°N) and Jicamarca (dip lat. 0.5°N), has demonstrated that ESF dynamics has distinct similarities and differences regardless of separation distance. This confirms the assertion by Pezzopane et al., (2013) that there exist seasonal variations in ESF over different equatorial stations separated in longitudes and latitudes.

CHAPTER SIX

CONCLUSION

We have shown in this study that there exists a well pronounced seasonal variability of ESF over Puerto Maldonado. Both pre-MN and post-MN events recorded high occurrences of about 80-100% during the summer months (November, December, January, & February), and a minimum of about 25% during the winter months (May, June, July, & August). We also noted that summer equinox (March & April) generally registered a higher ESF prevalence compared to winter equinox (September & October). Similarly, summer solstice (December & January) recorded higher ESF prevalence than the winter solstice (June & July). The physical mechanisms behind the variations in seasonal prevalence can be qualitatively explained by GWBA theory and the seasonal ITCZ migration influence on gravity-wave seeding which initiates RT-instability as championed by Tsunoda (2010). The seasonal ESF variability observed at Puerto Maldonado overall shows a similar trend to those reported at Jicamarca and Trivandrum, however, there are significant quantitative differences in ESF occurrences at these stations. We have further shown that the daytime vertical plasma drift, post-sunset PRE, and increase in solar flux influences ESF occurrence.

The ESF onset times and persistence for pre-MN ESF were found to be distinctively different from those of post-MN epochs. Pre-MN ESF occurrences lasted for about ~7 hours averaged for summer months compared to values of about ~3 hours recorded for winter months. On the contrary, the monthly averaged duration for post-MN ESF was about 1-2 hours longer than the pre-MN occurrence duration in winter. Winter months also registered late onset time compared to summer months by up to a maximum of about 5 hours a phenomenon thought to be duet to over-exposition of electrons to the meridional polarization drifts by weak PRE therefore

extending the lifetime of the few occurring spread events towards dawn (Somoye, 2010). It was further noted that the monthly average spread ranges were longer during summer months depicting very high intensity of ESF while the winter months registered very low values of spread ranges with an exception in June when abnormally high ranges were seen. This is thought to be due to the effect of frequent appearance of sporadic-E causing eastward polarization of electric field (Yizengaw, et al., 2013).

The negative daytime $\mathbf{E} \times \mathbf{B}$ drift, was also noted to last 3 hours longer in summer solstice (0700-1600 LT) than in winter solstice (0900-1500 LT) and is most intense during equinoctial months and is thought to be partly the reason behind the early onset of pre-MN ESF during summertime. The PRE drift commenced between 1600 LT and around 1900 LT when it attains a threshold vertical drift of ~30m/s coinciding with the average onset time of pre-MN ESF. This phase lasts longest (but is weaker) in winter solstice than in summer solstice thus exuding a solsticial asymmetry like that of ESF prevalence. The post-MN ESF is thought to be initiated by nighttime reversal of electric field (Risbeth, 2000), which coincides with the midnight drift reversal. We therefore confirm that the magnitude of post-sunset PRE drift and the daytime drifts both have an influence on ESF prevalence and persistence.

We also report a weak positive but significant correlation between solar flux observations and the ESF percentage occurrence values and a weak inverse correlation between solar flux and ESF spread range (ESF intensity) during both pre-MN and post-MN epochs. These results are in agreement with (Cueva et, 2013) observations, but contradicts those reported by Chapagain et al., (2012). Summer months with the highest foF2 values experienced the most intense spreading of the ionogram traces and the highest prevalence of ESF during both pre-MN and post-MN epochs. However, we also noted that wintertime is characterized by low critical frequencies and

57

therefore highly depleted ionospheric electron densities coinciding with low ESF prevalence and high post-MN ESF durations.

To sum up, we have found that the ESF variability at Puerto Maldonado is unique and does not replicate exactly those observed at other stations in South American and Indian region. We have shown the roles of major ESF drivers: solar flux, ExB plasma drift, and ambient electron density. Using a combination of a number of physical mechanisms proposed by different authors (GWBA hypothesis, PRE effects, sporadic E and westward electric field) it is possible to explain most of the peculiarities of the ESF occurrence at Puerto Maldonado. This makes it possible to outline the possibility for forecasting ESF at this location.

CHAPTER SEVEN

RECOMMENDATIONS

7.1 Possible Applications

We recommend that the seasonal variations of ESF noted in this study be observed by HF radio communication industry and navigation systems when planning routine diurnal and annual operations. For instance, they should note that pre-midnight periods experience high ESF prevalence and intense spreading during summertime and therefore alternatives to trans-ionospheric modes may prove more reliable as compared to wintertime. The observed foF2 trend also implies that, radio frequencies of about 9.5 MHz may be useful during pre-MN hours as opposed to post-MN periods when the electron densities have drastically reduced, more so during winter times. Furthermore, they can also use both daytime drift and PRE drift observations to monitor the post-sunset ESF occurrence. Finally, they need to note that solar flux increase inhibits spread intensity (with an exception in June solstice) but enhances its occurrence so radio signals will be adversely affected during low solar flux when spread is more intense than during high solar flux epochs.

7.2 Further Research

Even though this study is based on an entire year's observations, it is felt that the duration may still not be sufficient enough to model these observed seasonal characteristics and dynamics of the ionosphere above Puerto Maldonado over a complete solar cycle. Therefore, we recommend a climatology study that will span over 11 years to capture the varying intrigues of the ionosphere through the entire solar cycle and to further establish the inhibition of ESF intensity during high solar flux conditions. We further recommend similar analysis of pre- and post-MN ESF over other stations in South American region to compare to the findings reported

59

in this work. It certainly will be very interesting to conduct this kind of study in Equatorial Africa, namely using the Maseno VIPIR ionosonde which can now provide a benefit of routine observations in this region.

REFERENCES

Abdu, M. A. (2012). Equatorial spread-F development and quiet time variability under solar minimum conditions. *Indian Journal of Radio & Space Physics, 41*, 168-183.

Babiu, A. B., Mamukuyomi, A. I., and Joshua, E. O. (2007). Variability of equatorial ionosphere inferred from geomagnetic field measurements. *Bulletin of Astronomical Society of India, 35*, 607-618.

Basu, B. (1997). Generalized Rayleigh-Taylor instability in the presence of time-dependent equilibrium, *Journal for Geophysical Research, 102*, 17305-17312.

Bhattacharya, A. B. 7 and Pandit, J. (2014). Seasonal variations of spread-F occurrence probability at low-latitude and its relation with sunspot number. *International Journal on Electronics and Communication Technology, Vol. 5*, SPL-2.

Bibl, K. (1998). Evolution of the ionosonde. *Annals of Geophysics, Vol. 4*, N. 5-6.

Buchert, S. (2007). *Introduction to ionospheric physics*. Mariehamn: Finland.

Bullet, T. (2011). *High frequency radars and ionospheric sounding*. Retrieved 7th August, 2015 from, http://www.ngdc.noaa.gov/ftp/ionosonde/documentation/VIPIR/Ionospheric_

Bullet, T. (2013). *VIPIR ionosonde: Field site requirements*. Retrieved 5th August, 2015 from, http://www.ngdc.noaa.gov/ftp/ionosonde/documentation/VIPIR/VIPIR_Site_Needs-Mar13.pdf

Bullet, T., Malagnini, A., Pezzopane, M., and Scotto, C. (2010). Application of Autoscala to ionograms recorded by the VIPIR ionosonde. *Advances in Space Research, 45*, 1156-1172.

Candido, C., Batista, I., Becker-Guedes, F., Abdu, M., Sobral, J. H., and Takahashi, H. (2011). Statistical analysis of spread-F occurrence and ionospheric variability over Brazil during solar minimum activity. *Geophysical Research Abstracts, Vol. 13*, EGU2011-4453.

Carrano, C. S. and Groves, K. M. (2010). Temporal decorrelation of GPS satellite signals due to multiple scattering from ionospheric irregularities. *Proceedings of the Institute of Navigation ION GNSS meeting 21–24 June*. Portland, OR.

Chapagain, N. P. (2011). *Dynamics of equatorial spread-F using ground-based optical and radar measurements*. (Graduate Theses and Dissertations). Digital Commons Database. (Paper 897). Retrieved 12th June 2014 from http://digitalcommons.usu.edu/etd/897

Chapagain, N. P., Fejer, B. G., and Chau, J. L. (2009). Climatology of postsunset equatorial spread-F over Jicamarca. *Journal of Geophysical Research, 114*, A07307, doi:10.1029/2008JA013911

Chen, W. S., Liu, J. Y., Lee, C. C., Reinisch, B. W., and Chu, F. D. (2004). The effects of the pre-reversal E×B drift, the EIA asymmetry, and magnetic activity on the equatorial spread-F during solar maximum. Journal of Geophysical Research, 114, 10834-11432.

Clette, F. (2015). *2014: Maximum year for solar cycle 24*. Retrieved 10th August from, http://www.sidc.be/silso/news004

Cueva, R.Y.C., Paula, E.R., and Kherani, A.E. (2013). Statistical analysis and modeling of equatorial spread F parameters obtained from VHF radar at three longitudinal sectors. *13th International Congress of the Brazilian Geophysical Society & EXPOGEF,* pp. 1889-1896. doi: 10.1190/sbgf2013-389

Dabas, R. S., Das, R. M., Sharma, K., Garg, S. C., Devasia, C. V., Subbarao, K. S. V., Niranjan, K., and Rao, P. V. (2007). Equatorial and low latitude spread-F irregularity characteristics over the Indian region and their prediction possibilities. *Journal of Atmospheric and Solar-Terrestrial Physics, 69,* 685–696.

Davies, K. (1989). *Ionospheric radio*. London: Peter Peregrinus Ltd.

Emerson, D. (1998). *Elliptical polarization in the ionosphere.* Retrieved 12th August, 2015 from https://www.cv.nrao.edu/~demerson/ionosphere/ionopol.html

Engavale, B., Jeeva, K., Nair, K., and Bhattacharyya, A. (2005). Solar flux dependence of coherence scales in scintillation patterns produced by ESF irregularities. *Annales Geophysicae, 23,* 3261-3266.

Fejer, B. G., Scherliess, L., and de Paula, E. R. (1999). Effects of the vertical plasma drift velocity on the generation and evolution of equatorial spread-F. Journal of Geophysical Research, 104, 19859-119869.

Gentile, L. C., Burke, W. J., and Rich, F. J. (2006). A global climatology for equatorial plasma bubbles in the topside ionosphere. *Annals of Geophysics, 24,* 163-172.

Grubb, R. N., Livingston, R., and Bullet, T. W. (2008). *A new general purpose high-performance (HF) radar.* URSI General Assembly, August 7-16, Chicago (Paper GH-4).

Joyce, G. and Krall, J. (2012) Three-dimensional equatorial spread F modeling. *Geophysical Research Letters*, 35, L10102. doi: 10.1029/2008GL033509.

Krishna, G. S., Valladares, C. E., Doherty, P., Bullet, T., and Livingston, R. (2011). *Studies of equatorial spread-F using LISN VIPIR*. Retrieved on 5th August, 2015 from, http://lisn.igp.gob.pe/files/papers_lisn/Gopi_Seemala.pdf

Liu, L. and Wan, W. (2001). Evolution of equatorial trough of ionospheric F-region ionization. *Terrestrial Atmospheric and Oceanic Sciences, Vol. 12*, No. 3, 559-565.

Manju, G., Madhav, M. K., Ramkumar, G., Pant, T.K., Sridharan, R. Sreelatha, P. ... and Ram, T. S. (2012). Equinoctial asymmetry in the occurrence of equatorial spread-F over Indian longitudes during moderate to low solar activity period 2004 – 2007. *Indian Journal of Radio & Space Physics, Vol. 41*, pp 240-246.

Mc Danile, (2009). *A review of equatorial spread-F*. National Oceanic and Atmospheric Administration (NOAA). *Ionospheric sounding and VIPIR operation*. Retrieved 10th August from, ftp://ftp.ngdc.noaa.gov/ionosonde/documentation/VIPIR/

Oyekola, O. S., and Oluwafemi, C. O. (2009). A study of evolution/suppression parameters of equatorial post-sunset plasma instability. *Annals of Geophysics, 27*, 297-301.

Paznukhov, V. V., Carrano, C. S., Doherty, P. H., Groves, K. M., Caton, R. G., Valladares, G. K., ..., and Tsidu, G. M. (2012). Equatorial plasma bubbles and L-band scintillations in Africa during solar minimum. *Annals of Geophysics, 30*, 675–682.

Pezzopane, M., Zuccheretti, E., Abadi, P., de Abreu, J., de Jesus, R., Fagundes, R., ... , and Ezquer, G. (2013). Low-latitude equatorial spread-F occurrence at different longitude sectors under low solar activity. *Annals of Geophysics, 31*, 153-162.

Poole, I. (n.d.) *The Ionosphere and Radio Wave Propagation*. Retrieved 12th June 2014 from, http://www.radio-electronics.com/info/propagation/ionospheric/ionosphere.php

Ram, S. T., Rao, P. S., Niranjan, K., Prasad, D. V., Sridharan, R., Devasia, C., and Ravindran, S. (2006). Role of post-sunset vertical drifts at the equator in predicting the onset of VHF scintillations during high and low sunspot activity years. *Annales Geophysicae, 24*, 1609-1616.

Rao, P. V. S., Ram, T. S., Niranjan, K., and Prasad, D.V. (2006). The role of post sunset vertical drifts at the equator in predicting the onset of VHF scintillations during high and low sunspot activity years. *ILWS Workshop 19-24, February*, GOA.

Rees, M. H. (1989). *Physics and chemistry of the upper atmosphere*. New York (NY): Cambridge University Press.

Risbeth, H., (2000). The equatorial F-layer: progress and puzzles. *Annales Geophysicae, 18*, 730-739.

Sastri, J. H. (1983) Duration of equatorial spread-F. *Indian Institute of Astrophysics.* Retrieved 12th June 2014 from, http://prints.iiap.res.in/bitstream/2248/3824/3/Duration%20of%20 equatorial%20spread-F.pdf

Schunk, R. W. and Nagy, F. A. (2009). *Ionospheres: Physics, Plasma Physics and Chemistry.* New York: Cambridge University Press.

Shi, J. K., Tao, W., Wang, G. J., Zherebotsov, G., Pirog, O., and Stepanov, A. (2011). Properties of spread-F in high and low latitude ionospheres. *Progress in Electromagnetics Research Symposium Proceedings 20–23, March.* Marrakesh: Morocco.

Somoye, E. O. (2010). Diurnal and seasonal variation of fading rates of E- and F-region echoes during IGY and IQSY at the equatorial station of Ibadan. Indian Journal of Radio & Space Physics, Vol. 38, pp. 194-202.
Sounding-ASEN-5245.pdf

Stolle, C., Luhr, H. L., and Fejer, B. G. (2008). Relation between the occurrence rate of ESF and the equatorial vertical plasma drift velocity at sunset derived from global observations. Annals of Geophysics, 26, 3979–3988.

Sultan, P. J. (1996). Linear theory and modeling of the Rayleigh-Taylor instability leading to the occurrence of equatorial spread-F. *Journal for Geophysical Research, 101*, 26875-26891.

Titheridge, J. E. (1998). The real height analysis of ionograms: A generalized formulation. *Radio Science, 23*, 831-849.

Tsunoda, T. R. (2010). On seeding equatorial spread F during solstices: *Geophysical Research Letters, Vol. 37*, L05102. doi:10.1029/2010gl042576

Valladares, C. and Chau, J. (2012). The Low-latitude Ionosphere Sensor Network (LISN): Initial results. *Radio Science, Vol. 47*, RS0L17. doi:10.1029/2011RS004978

Valladares, C. E. and Doherty, P. H. (2011). Identification of TIDs and plasma depletions using the LISN observatory. Institute of Electrical and Electronic Engineers. doi: 10.1109/URSIGASS.2011.6050907

Wyman, G. (2009). Characterizing the ionosphere. *NATO Science and Technology Organization, TRO-TR-IST-05.* ISBN 978-92-837-0057-9

Xenos, T. D. (2002). The effects of foF2 variability on TEC prediction accuracy. *Annals of Geophysics,* Vol. 45, N.

Yizengaw, E., Moldwin, B., Sahai, Y., and de Jesus, R. (2009). Strong post-midnight equatorial ionospheric anomaly. *Journal of Geophysical Research, 114,* A12308. doi:10.1029/2009JA014603.

Yizengaw, E., Retterer, J., Pacheco, E., Roddy, P., Groves, K., Caton, R., ..., and Stoneback, R. (2013). *Post-midnight bubbles and scintillations in the quiet-time June solstice: Possible forcing from lower atmosphere.* Retrieved 12th August, 2015 from, http://scostep.apps01.yorku.ca/wpcontent/uploads/2014/10/YizengawE_Session7_1_STP13.pdf

Zalesak, S. T. and Ossakow, S. L. (1982). On the prospect for artificially inducing equatorial spread-F. *Navigation Research Laboratory,* Rep, 4899.

Zolesi, B. and Cander, R. L. (2014). Ionospheric prediction and forecasting. *Springer Geophysics.* doi: 10.1007/978-3-642-38430-1_2